Supplementary Information (SI)

Investigating the Validity of the Knudsen Diffusivity Prescription for Mesoporous and Macroporous Materials

Rajamani Krishna

Van 't Hoff Institute for Molecular Sciences, University of Amsterdam, Science Park 904,

1098 XH Amsterdam, The Netherlands

*CORRESPONDING AUTHOR Tel +31 20 6270990; Fax: + 31 20 5255604;

email: r.krishna@contact.uva.nl

Table of Contents

1. Preamble

This Supporting Information (SI) accompanying the article *Investigating the Validity of the Knudsen Diffusivity Prescription for Mesoporous and Macroporous Materials* provides (a) detailed comparisons of the Dusty Gas, and the Maxwell-Stefan models for mesopore and macropore diffusion, (b) details of the Veldsink, Tuchlenski, and Yang experiments for transient mixture permeations, (c) details of the numerical solutions to the equations describing transient mixture diffusion across membranes, (d) input data on the parameters used to model Tuchlenski, Yang and, and Veldsink experiments, and (e) detailed comparisons of experimental data with model simulations.

For ease of reading, this Supplementary Material is written as a stand-alone document; as a consequence, there is some overlap of material with the main manuscript.

2. The Dusty Gas Model for mixture diffusion

For *n*-component diffusion in a cylindrical pore, the DGM flux relations are commonly written as[1]

$$-\varepsilon\frac{p_t}{RT}\frac{\partial x_i}{\partial z}-\varepsilon\left(\frac{x_i}{RT}\right)\left(\frac{B_0 p_t}{\eta D_{i,Kn}}+1\right)\frac{\partial p_t}{\partial z}=\sum_{\substack{j=1\\ j\neq i}}^{n}\left(\frac{x_j N_i - x_i N_j}{Đ_{ij}}\right)+\frac{N_i}{D_{i,Kn}};\quad i=1,2...n \tag{1}$$

The fluxes N_i are defined as the moles transported per m^2 of total external surface area of the porous material

$$N_i \equiv \varepsilon\frac{p_i}{RT}u_i;\quad i=1,2...n \tag{2}$$

The species velocities u_i are defined in a reference framework with respect to the pore walls. The porosity ε appears on the left member of equation (2) because only a fraction ε of the external surface is available for influx of guest molecules.

Equation (1) combines the contributions to the fluxes N_i arising from (a) molecule-wall collisions, reflected in the Knudsen diffusivity, $D_{i,Kn}$, (b) molecule-molecule collisions , reflected in the bulk gas

phase diffusivity, $Đ_{ij}$, and (c) viscous flow with the permeability coefficient B_0; see schematic in Figure 1 that is adapted from Mason and Malinauskas.[1]

The bulk gas phase diffusivities $Đ_{ij}$ for a *binary* mixture of species *i* and species *j* can be estimated using the kinetic theory of gases or from empirical procedures such as the Fuller-Schettler-Giddings method.[2, 3] These values are the same for the *i* - *j* combination in an *n*-component mixture. For ideal gas mixtures, the bulk gas phase diffusivities are inversely proportional to the pressure.

For a cylindrical pore of diameter d_p, the permeability B_0 is

$$B_0 = \frac{d_p^2}{32} \tag{3}$$

The Knudsen prescription is

$$D_{i,Kn} = \frac{d_p}{3}\sqrt{\frac{8RT}{\pi M_i}} \tag{4}$$

The formula (4), that was first put forward by Knudsen[4] and subsequently refined by Smoluchowski,[5] needs further elucidation. Equation (4) is based on the assumption that the reflections of a molecule after collision with the pore wall are purely *diffuse* in nature, i.e. the angle of reflection bears no relation to the angle of incidence at which the molecule strikes the pore wall.

In order to get an appreciation of the relative importance of molecule-wall and molecule-molecule interactions, Figure 2a presents a comparison Knudsen ($D_{He,Kn}$, $D_{Ar,Kn}$), and bulk diffusivities ($Đ_{He,Ar}$) of He/Ar mixtures at 293 K in cylindrical mesopores and macropores. The calculations of the bulk diffusivities $Đ_{He,Ar}$ are at total pressures of 0.1 MPa. These results show that, generally speaking, diffusion in mesopores is dominated by molecule-wall collisions.

Increasing the system pressure, lowers the bulk diffusivities and therefore molecule-molecule collisions become of increasing importance for high pressure operations. Figure 2b compares the Knudsen ($D_{He,Kn}$, $D_{Ar,Kn}$), and bulk diffusivities ($Đ_{He,Ar}$) of He/Ar mixtures at 293 K for a mesopore of

10 nm, at varying system pressures. At pressures above 2 MPa, the molecule-molecule collisions become comparable in importance as molecule-wall collisions.

For non-cylindrical pores, with tortuosity τ, the DGM are re-written in the form

$$-\frac{p_t}{RT}\frac{\partial x_i}{\partial z}-\left(\frac{x_i}{RT}\right)\left(\frac{B_0 p_t}{\eta D_{i,Kn}}+1\right)\frac{\partial p_t}{\partial z}=\sum_{\substack{j=1\\ j\neq i}}^{n}\left(\frac{x_j N_i - x_i N_j}{(\varepsilon/\tau)Đ_{ij}}\right)+\frac{N_i}{(\varepsilon/\tau)D_{i,Kn}};\quad i=1,2...n \tag{5}$$

It is common practice to define "effective" coefficients

$$D^e_{i,Kn}=(\varepsilon/\tau)D_{i,Kn};\quad Đ^e_{ij}=(\varepsilon/\tau)Đ_{ij};\quad B^e_0=(\varepsilon/\tau)d_p^2/32;\quad B^e_0/D^e_{i,Kn}\equiv B_0/D_{i,Kn} \tag{6}$$

and re-write equation (5) as

$$-\frac{p_t}{RT}\frac{\partial x_i}{\partial z}-\left(\frac{x_i}{RT}\right)\left(\frac{B_0 p_t}{\eta D_{i,Kn}}+1\right)\frac{\partial p_t}{\partial z}=\sum_{\substack{j=1\\ j\neq i}}^{n}\left(\frac{x_j N_i - x_i N_j}{Đ^e_{ij}}\right)+\frac{N_i}{D^e_{i,Kn}};\quad i=1,2...n \tag{7}$$

For a cylindrical pore, the tortuosity τ=1 and equation (7) reduces to equation (1).

Summing equation (7) over all the *n*-species we obtain

$$-\frac{1}{RT}\left(1+\frac{B_0 p_t}{\eta}\sum_{i=1}^{n}\frac{x_i}{D_{i,Kn}}\right)\frac{\partial p_t}{\partial z}=\sum_{i=1}^{n}\frac{N_i}{D^e_{i,Kn}} \tag{8}$$

The term $\frac{B_0 p_t}{\eta}\sum_{i=1}^{n}\frac{x_i}{D_{i,Kn}}$ indicates the fractional contribution of viscous flow to the changes in the total pressure.

For the DGM model, we define the square matrix [*B*]

$$[B]=\begin{bmatrix}\frac{1}{D^e_{1,Kn}}+\frac{x_2}{Đ^e_{12}} & -\frac{x_1}{Đ^e_{12}}\\ -\frac{x_2}{Đ^e_{12}} & \frac{1}{D^e_{2,Kn}}+\frac{x_1}{Đ^e_{12}}\end{bmatrix};\quad \text{DGM model} \tag{9}$$

Equation (7) can be re-cast into 2-dimensional matrix notation for explicit evaluation of the fluxes

$$\begin{pmatrix} N_1 \\ N_2 \end{pmatrix} = -\frac{1}{RT}[B]^{-1} \begin{pmatrix} \frac{\partial p_1}{\partial z} + x_1\left(\frac{B_0 p_t}{\eta D_{1,Kn}} + 1\right)\frac{\partial p_t}{\partial z} \\ \frac{\partial p_2}{\partial z} + x_2\left(\frac{B_0 p_t}{\eta D_{2,Kn}} + 1\right)\frac{\partial p_t}{\partial z} \end{pmatrix}; \quad \text{DGM model} \tag{10}$$

For mixtures of non-adsorbing gases such as He-Ar, the DGM equations (7) are in good agreement with experimental data.[1, 6]

In practice, the guest molecules have finite adsorption on the pore walls. In the DGM model concept as put forward by Mason and Malinauskas,[1] the motion of adsorbed molecules along the surface of the pore walls needs to be accounted for as an additional, parallel, contribution; see schematic in Figure 1. The surface diffusion contribution is appropriately described in the Maxwell-Stefan (M-S) formulation[7, 8]

$$N_{i,surface} = -Đ_{i,s}\frac{c_i}{RT}\frac{d\mu_i}{dz}; \quad i = 1,2...n \tag{11}$$

In equation (11), c_i is the molar concentration of species *i* in the *adsorbed* phase expressed in terms of moles per m^3 of the accessible pore volume, μ_i is the chemical potential of species *i* in the adsorbed phase, and $Đ_{i,s}$ is the M-S surface diffusivity of species *i*. It is convenient to re-write Equation (11) in terms of the gradients in the molar concentrations of the components in the adsorbed phase. Towards this end, we define a matrix of thermodynamic factors Γ_{ij}

$$\frac{c_i}{RT}\frac{\partial \mu_i}{\partial z} = \sum_{j=1}^{n}\Gamma_{ij}\frac{\partial c_i}{\partial z}; \quad \Gamma_{ij} = \frac{c_i}{p_i}\frac{\partial p_i}{\partial c_j}; \quad i, j = 1,2,,n \tag{12}$$

and so

$$N_{i,surface} = -Đ_{i,s}\sum_{j=1}^{n}\Gamma_{ij}\frac{dc_j}{dz}; \quad i = 1,2...n \tag{13}$$

Most commonly, the surface diffusivity decreases with surface coverage

$$Đ_{i,s} = Đ_{i,s}(0)(1 - \theta_1 - \theta_2 - .... - \theta_n) \tag{14}$$

Since there are no predictive methods for estimation of the surface diffusivities in equation (11), experimental data are required.

The work of Tuchlenski et al.[9] provides an excellent account of how the DGM equation (7) can be combined with the M-S equation (11) for surface diffusion[7, 8] in order to model transient mixture permeation across a Vycor glass mesoporous membrane of average pore diameter $d_p \approx 4$ nm. The surface diffusivities are fitted to match the experimental data on membrane permeation.

Wu et al.[10] develop a model to combine surface diffusion in shale reservoirs with the other flux contributions.

The DGM model formulation has been subject to criticism in the recent literature due to some inconsistencies in handling the viscous flow contribution.[11, 12]

3. The linearized solution to the DGM

For explicit calculations of the transfer fluxes, a linearization technique has been suggested by Krishna.[13] as explained below. The "linearization" procedure essentially involves the assumption that the matrix [B], defined in equation (9) for DGM, can be considered to be constant during the discretized time interval, provided it is evaluated at the average compositions $\bar{x}_1$ and $\bar{x}_2$ within the capillary membrane, of thickness δ.

The linearized DGM model yields

$$\begin{pmatrix} N_1 \\ N_2 \end{pmatrix} = \frac{1}{RT\delta}[B]^{-1} \begin{pmatrix} (p_{10} - p_{1\delta}) + \bar{x}_1 \left(\frac{B_0 p_t}{\eta D_{1,Kn}} + 1 \right) (p_{t0} - p_{t\delta}) \\ (p_{20} - p_{2\delta}) + \bar{x}_2 \left(\frac{B_0 p_t}{\eta D_{2,Kn}} + 1 \right) (p_{t0} - p_{t\delta}) \end{pmatrix} \tag{15}$$

This linearized procedure is used in all of the model calculations presented in this article. In order to verify the validity of the linearized procedure, we shall compare the calculations using equation (15) with the experimental data of Remick and Geankoplis.[14]

Remick and Geankoplis[14] have measured the fluxes of helium (1), neon (2) and argon (3) across a porous capillary diffusion cell made up of cylindrical capillaries of diameter d_p = 39.1 μm, and length δ

= 9.6 mm. The experiments were performed in such a way that the pressure drop across the capillary diffusion cell was zero, so that there was no viscous flow. The average system pressure, p_{av}, was varied and so were partial pressure driving forces, $p_{i0} - p_{i\delta}$; the data are tabulated in Table 1 of their paper.

Figure 3a presents a comparison of the experimental data (shown by symbols) of Remick and Geankoplis[14] for the fluxes of helium (1), neon (2) and argon (3) with the calculations using the linearized equation (15). There is very good agreement between the calculated fluxes and experimental data over the wide range of system pressures. With increasing pressure, the bulk gas phase diffusivities, $Đ_{ij}$, are reduced and molecule-molecule collisions become increasingly important. Conversely, molecule-wall collisions are important at lower pressures. The DGM correctly predicts the transition between Knudsen controlled and bulk diffusion controlled regimes. In the Knudsen regime, the transfer fluxes linearly proportional to the system pressure. In bulk diffusion regime, the transfer fluxes are independent of pressure.

Figure 3b presents calculations of the fluxes as a function of the capillary diameter, d_p, maintaining the total pressure = 10^3 Pa. Three regimes can again be distinguished. In the Knudsen regime, the flux is proportional to the capillary diameter, d_p. In the bulk diffusion regime, the flux is independent of the pore diameter.

4. The Dusty Gas Model (DGM) for unary diffusion

For unary diffusion, the total contributions of Knudsen diffusion, surface diffusion, and viscous flow are

$$N_i = -\frac{1}{RT}\left(\frac{B_0 p_i}{\eta_i D_{i,Kn}} + 1\right) D^e_{i,Kn}\frac{dp_i}{dz} - Đ_{i,s}\frac{c_i}{RT}\frac{d\mu_i}{dz} \tag{16}$$

The chemical potential gradients can be related to the gradients of the molar concentrations in the adsorbed phase by introducing the thermodynamic factor Γ_i

$$\frac{c_i}{RT}\frac{d\mu_i}{dz} = \Gamma_i \frac{dc_i}{dz}; \quad \Gamma \equiv \frac{c_i}{p_i}\frac{\partial p_i}{\partial c_i} \tag{17}$$

For mono-layer Langmuir adsorption,

$$\theta_i = \frac{c_i}{c_{i,sat}} = \frac{b_i p_i}{1 + b_i p_i}; \quad \Gamma_i = \left(1 + b_i p_i\right) = \frac{1}{1 - \theta_i} \tag{18}$$

where θ_i is the fractional surface coverage. The fractional vacancy, θ_V, is

$$\theta_V = 1 - \theta_i = \frac{1}{1 + b_i p_i} \tag{19}$$

Differentiating the Langmuir Equation (18), we can write

$$\frac{dc_i}{dz} = \frac{c_{i,sat} b_i}{\left(1 + b_i p_i\right)^2} \frac{dp_i}{dz} \tag{20}$$

Combining Equations (14), (16), (18), and (20) we obtain

$$N_i = -\frac{1}{RT}\left(\frac{B_0 p_i}{\eta_i D_{i,Kn}} + 1\right) D^e_{i,Kn} \frac{dp_i}{dz} - Đ_{i,s}(0) \frac{c_{i,sat} b_i}{\left(1 + b_i p_i\right)} \frac{dp_i}{dz} \tag{21}$$

We shall illustrate the use of equation (21) to calculate the fluxes. Figure 4 shows the unary CO_2 permeation fluxes across Vycor glass membrane at (a) 293 K, and (b) 343 K as a function of upstream pressure (keeping the downstream pressure constant at 101 kPa). Also shown in Figure 4 are the calculations neglecting the contribution of the second member on the right hand side of the equality. Figure 4 shows that the DGM concept anticipates a slight enhancement of the flux due to surface diffusion.

5. The Maxwell-Stefan model for mesopore diffusion

In recent works, a different approach to the description of diffusion in porous materials has been developed, using the Maxwell-Stefan approach,[15-19] employing chemical potential gradients as driving forces:

$$-\rho V_p \frac{c_i}{RT} \frac{\partial \mu_i}{\partial z} = \sum_{\substack{j=1 \\ j \neq i}}^{n} \left(\frac{x_j N_i - x_i N_j}{Đ_{ij}}\right) + \frac{N_i}{Đ_i}; \quad i = 1,2...n \tag{22}$$

In equation (22), c_i is the molar concentration of species *i* based on the accessible pore volume, V_p (= m^3 pore volume per kg framework), and ρ is the material framework density. The quantity ρV_p is the fractional pore volume

$$\rho V_p = \left(\frac{\text{kg framework}}{\text{m}^3 \text{ framework}}\right)\left(\frac{\text{m}^3 \text{ pore volume}}{\text{kg framework}}\right) = \left(\frac{\text{m}^3 \text{ pore volume}}{\text{m}^3 \text{ framework}}\right) = \varepsilon \tag{23}$$

Equation (22) applies to microporous, mesoporous, and macroporous materials. For mesoporous, and macroporous materials with the fluid phase in the gaseous state, $c_i = \frac{p_i}{RT}; \quad \frac{\partial \mu_i}{\partial z} = \frac{RT}{p_i}\frac{\partial p_i}{\partial z}$, the left hand side of equaton (22) simplifies to yield

$$-\varepsilon \frac{1}{RT}\frac{\partial p_i}{\partial z} = \sum_{\substack{j=1 \\ j\neq i}}^{n}\left(\frac{x_j N_i - x_i N_j}{Đ_{ij}}\right) + \frac{N_i}{Đ_i}; \quad i = 1,2...n \tag{24}$$

For pores with tortuosity τ, equation (24) may be modified as follows

$$-\frac{1}{RT}\frac{\partial p_i}{\partial z} = \sum_{\substack{j=1 \\ j\neq i}}^{n}\left(\frac{x_j N_i - x_i N_j}{(\varepsilon/\tau)Đ_{ij}}\right) + \frac{N_i}{(\varepsilon/\tau)Đ_i}; \quad i = 1,2...n \tag{25}$$

and is comparable, but not equivalent with the corresponding DGM equation (5). In the M-S formulation (25), the M-S diffusivity $Đ_i$ describes the interaction between species *i* and the pore wall. The Maxwell-Stefan diffusion formulation is essentially a "friction formulation"; the M-S diffusivity $Đ_i$, is to be interpreted as an inverse drag coefficient between the guest molecule and the surface of the framework material; this diffusivity reflects both the Knudsen and surface diffusion characteristics. In other words, the surface diffusion is not separately accounted for. Furthermore, any viscous flow contribution is also subsumed into the M-S diffusivities $Đ_i$, and $Đ_{ij}$. Comparing equation (25) with the DGM equation (1) we may derive; see Krishna and Wesselingh[20]

$$Đ_i = D_{i,Kn}\left(1 + \frac{B_0 p_t}{\eta}\sum_{j=1}^{n}\frac{x_j}{D_{j,Kn}}\right); \quad i = 1,2...n \tag{26}$$

For explicit evaluation of the fluxes, it is convenient to define a square matrix

$$[B]=\begin{bmatrix} \dfrac{1}{Đ_1(\varepsilon/\tau)}+\dfrac{x_2}{Đ_{12}(\varepsilon/\tau)} & -\dfrac{x_1}{Đ_{12}(\varepsilon/\tau)} \\ -\dfrac{x_2}{Đ_{12}(\varepsilon/\tau)} & \dfrac{1}{Đ_2(\varepsilon/\tau)}+\dfrac{x_1}{Đ_{12}(\varepsilon/\tau)} \end{bmatrix}; \quad \mathrm{M-S\ model} \tag{27}$$

Equation (25) may be re-written to enable explicit calculation of the fluxes

$$\begin{pmatrix} N_1 \\ N_2 \end{pmatrix} = -\frac{1}{RT}[B]^{-1}\begin{pmatrix} \dfrac{\partial p_1}{\partial z} \\ \dfrac{\partial p_2}{\partial z} \end{pmatrix}; \quad \mathrm{M-S\ model} \tag{28}$$

Figure 5a presents MD data on Maxwell-Stefan diffusivity $Đ_{12}$, for equimolar ($c_1 = c_2$) binary mixture of CH_4-Ar in silica pores with diameters in the range 2 nm to 10 nm. Also shown (square symbols) are the $Đ_{12,fl}$ data for binary fluid CH_4-Ar mixture diffusion, obtained from independent MD simulations. The molecule-molecule interactions are independent of the pore diameter, and equal the corresponding values of the fluid phase diffusivity. The straight line represents the estimations of the gas phase diffusivity $Đ_{12,fl}$ using the Fuller-Schettler-Giddings method.[2, 3] The results of Figure 5a indicate that the FSG method can be used to estimate the M-S diffusivity $Đ_{12}$ in cylindrical mesopores.

Figure 5b, c, d, e present MD data on the Maxwell-Stefan diffusivity $Đ_{12}$, for equimolar ($c_1 = c_2$) binary mixtures CO_2- CH_4, CH_4- H_2, CO_2- H_2, and Ar- H_2 in BTP-COF, a covalent organic framework with 3.4 nm hexagonal channels. The values are comparable in magnitude with corresponding values of the $Đ_{12,fl}$ data for binary fluid mixture diffusion, obtained from independent MD simulations.

Extensive data set of MD simulations for mesoporous channels show that the M-S diffusivity $Đ_i$ equals the Knudsen diffusivity value given by equation (4) for gases such as H_2 that have poor adsorption strength.[15-19, 21-23] For gaseous molecules that have finite adsorption on the pore walls, the M-S diffusivity $Đ_i$ is significantly lower than the value predicted by equation (4). The reasons for this departure must be attributed to the failure of the Knudsen formula for molecules with strong adsorption strength; this failure has been highlighted in several recent publications.[15-19, 21-23] Adsorption causes the

molecules to bind to the wall, and perhaps hop to a neighboring adsorption site, rather than return to the bulk after collision; this introduces a *bias* in the molecular hops. This bias increases with increasing adsorption strength, causing a violation of the diffuse reflectance assumption that is invoked in deriving equation (4).[17, 21, 22] It has been demonstrated that the departures from the Knudsen formula correlates with the binding energy for adsorption of the molecules at the pore walls.[23]

As illustration, Figure 6a presents MD data[23, 24] on the M-S diffusivity $Đ_i$ for various guest molecules (hydrogen, argon, carbon dioxide, methane, ethane, propane) in BTP-COF, that has 3.4 nm hexagonal channels, plotted as function of the pore concentration, c_i. The M-S diffusivities show a slight increase with increasing pore concentration. In the limit of zero-pore concentration, we denote the value of the diffusivity as $Đ_i(0)$. Figure 6b presents the values of $Đ_i(0)/D_{i,Kn}$ for BTP-COF, where the Knudsen diffusivity is estimated using equation (4). The $Đ_i(0)/D_{i,Kn}$ values range from approximately unity for H_2 to a value of 0.1 for n-hexane (nC6). Furthermore, $Đ_i(0)/D_{i,Kn}$ is seen to correlate very well with the Henry coefficient for adsorption. This is a rational result. The higher the binding energy, the higher is the sticking tendency of that species with the pore wall, leading to greater departure from the Knudsen prescription of diffuse reflectance.

Figure 6c presents a plot of the $Đ_i(0)/D_{i,Kn}$ for linear alkanes as a function of carbon number in BTP-COF, 2 nm cylindrical silica pore, and 3 nm cylindrical pore. In all these mesoporous structures, the decrease in $Đ_i(0)/D_{i,Kn}$ with increasing carbon number is due to increased adsorption strength.

Figure 7 shows MD data of M-S diffusivity at zero-loading, $Đ_i$, of (a) CH_4, (b) Ar, (c) CO_2, and (c) C_3H_8 in zeolites, MOFs, and silica mesopores, plotted as a function of the pore dimension. The data has been culled from various MD simulation data sources.[15-17] We note that the MD data fall consistently below the values prescribed by the Knudsen formula. The guest molecules CO_2, and C_3H_8 are strongly adsorbed on the silica pore walls, and the M-S diffusivity is significantly lower than then Knudsen diffusivity value.

6. The linearized solution to the M-S diffusion equations

Before analyzing the experimental data on meso- and macro-porous membranes, let us gain some insights into the relative importance of molecule-wall, molecule-molecule interactions in meso- and macro-porous materials.

For this purpose we analyze, and model, the two-bulb diffusion experiments of Duncan and Toor[25] with ternary $H_2(1)/N_2(2)/CO_2(3)$ gas mixtures. The experimental set-up consisted of a two bulb diffusion cells, pictured in Figure 8. The two bulbs were connected by means of capillary tube of length $\delta = 86$ mm, with a diameter, $d_p = 2.08$ mm. The total system pressures in either bulb at the start of the experiment is $p_{t0,A} = p_{t0,B} = 10^5$ Pa. At time $t = 0$, the stopcock separating the two composition environments at the center of the capillary was opened and diffusion of the three species was allowed to take place.

The initial compositions (mole fractions in the two bulbs, Bulb A and Bulb B), are

$$\begin{aligned} &\text{Bulb A}: x_{10,A} = 0.00000; x_{20,A} = 0.50086; x_{30,A} = 0.49914 \\ &\text{Bulb B}: x_{10,B} = 0.50121; x_{20,B} = 0.49879; x_{30,B} = 0.00000 \end{aligned} \tag{29}$$

The initial partial pressures in the two bulbs are

$$\begin{aligned} &\text{Bulb A}: p_{i0,A} = x_{i0,A} p_{t0,A} \\ &\text{Bulb B}: p_{i0,B} = x_{i0,B} p_{t0,B} \end{aligned} \tag{30}$$

The final equilibrated partial pressures will be equal in both bulbs

$$p_{i,eq} = \frac{p_{i0,A} + p_{i0,B}}{2} \tag{31}$$

The composition trajectories for each of the three diffusing species in either bulb has been presented in Figure 9. We note that despite the fact that the driving force for nitrogen is practically zero, it does transfer from one bulb to the other, exhibiting over-shoot and under-shoot phenomena when approaching equilibrium. The transient equilibration trajectories of H_2, and CO_2 are "normal", with their compositions in the two bulbs approaching equilibrium in a monotonous manner.

Let us now model the experiments. The flux relations are given by the Maxwell-Stefan equations (24):

$$
\begin{aligned}
-\frac{1}{RT}\frac{dp_1}{dz} &= \frac{x_2 N_1 - x_1 N_2}{Đ_{12}} + \frac{x_3 N_1 - x_1 N_3}{Đ_{13}} + \frac{1}{Đ_1};\\
-\frac{1}{RT}\frac{dp_2}{dz} &= \frac{x_1 N_2 - x_2 N_1}{Đ_{12}} + \frac{x_3 N_2 - x_2 N_3}{Đ_{23}} + \frac{1}{Đ_2};\\
-\frac{1}{RT}\frac{dp_3}{dz} &= \frac{x_1 N_3 - x_3 N_1}{Đ_{13}} + \frac{x_2 N_3 - x_3 N_2}{Đ_{23}} + \frac{1}{Đ_3}
\end{aligned}
\tag{32}
$$

We have omitted the porosity ε, because the N_i in equation (32) are defined in terms of the cross-sectional area of the cylindrical pore.

The M-S diffusivities for the three binary pairs at $T = 308.3$ K are (see Krishna[26] for further details)

$$
\begin{aligned}
Đ_{12} &= 8.33\times10^{-5} \quad \text{m}^2\ \text{s}^{-1}\\
Đ_{13} &= 6.8\times10^{-5} \quad \text{m}^2\ \text{s}^{-1}\\
Đ_{23} &= 1.68\times10^{-5} \quad \text{m}^2\ \text{s}^{-1}
\end{aligned}
\tag{33}
$$

The adsorption on the pore walls of the capillary tube are considered to be of negligible importance, and the Knudsen formula (4) is applied to calculate the M-S diffusivities $Đ_i$. In our simulations we ignore viscous flow contributions.

The transient partial pressures in Bulb A are given by

$$
V_{Bulb}\frac{1}{RT}\frac{\partial p_{i,A}(t)}{\partial t} = -A_{pore}N_i \tag{34}
$$

In equation (34), the flux is considered positive if directed from Bulb A to Bulb B. If we apply the linearization approach of Krishna,[13] and assume the matrix [B] (defined by equation (27), appropriately generalized), evaluated at the final equilibrated compositions, the set of equations (32) and (34) can be solved analytically to yield the 3-dimensional matrix differential equation describing the partial pressure transience in Bulb A, and Bulb B

$$\left(p_A(t)-p_{eq}\right)=\exp\left(-\frac{A_{pore}}{V_{Bulb}\delta}[B]^{-1}t\right)\left(p_{0,A}-p_{eq}\right)$$
$$\left(p_B(t)-p_{eq}\right)=\left(p_{eq}-p_A(t)\right) \tag{35}$$

For pore diameters, d_p larger than about 2 μm, the molecule-wall collisions are of negligible importance, and the diffusion is in the "bulk diffusion controlled regime". In this case, the simulation results in Figure 9 (shown by the continuous solid lines (for Bulb A) and dashed lines (for Bulb B)) are in excellent quantitative agreement with the experimental data of Duncan and Toor.[25] The overshoot experienced by nitrogen signifies uphill diffusion, as explained in considerable detail in earlier work.[26] The overshoots and undershoots experienced by nitrogen emanate from the differences in the binary pair M-S diffusivities of the constituent binary pairs $Đ_{12}, Đ_{13}, Đ_{23}$; see the values in equation (33).

Having established the accuracy of the M-S model to describe the transient diffusion for capillary diameters $d_p > 2$ μm, we proceed to examine two other scenarios: $d_p = 200$ nm (macropore), and $d_p = 2$ nm (mesopore); the simulation results are presented in Figure 10, and Figure 11.

For both these cases, the molecule-wall collisions are important. The inclusions of molecule-wall interactions leads to differences in the total pressures, $p_{t,A}$, anad $p_{t,B}$, in the two bulbs; see Figure 10b, and Figure 11b. These pressure overshoots are precisely analogous to those experienced in the Tuchlenski, Yang, and Veldsink membrane permeation experiments. The pressure overshoot is stronger for the mesopore capillary, $d_p = 2$ nm than for the macropore capillary $d_p = 200$ nm.

There is however, an important difference in the transient partial pressure equilibrations. For the $d_p = 200$ nm macropore, the overshoot and undershoot in the nitrogen partial pressures persists even with the inclusion of molecule-wall collisions; see Figure 10a. This implies that uphill diffusion phenomena can be experienced for mesopores; uphill diffusion arises because of the differences in the binary pair M-S diffusivities of the constituent binary pairs $Đ_{12}, Đ_{13}, Đ_{23}$.

For mesopore capillary, $d_p = 2$ nm, molecule-wall collisions are dominant and the contribution of molecule-molecule collisions is negligible. Therefore, no overshoots or undershoots are experienced by nitrogen during transient equilibration.

It is also interesting to examine the partial pressure profiles along the capillary tube at any instant of time, t. The analytic solution to the partial profiles as a function of distance, z, when two semi-infinite slabs are brought into contact with each other are given by (see the Supporting Information accompany the paper by Krishna[26])

$$\left(p(z,t)\right)=\frac{1}{2}\left(p_L+p_R\right)+\frac{1}{2}erf\left[-\frac{z}{\sqrt{4[B]^{-1}t}}\right]\left(p_R-p_L\right) \tag{36}$$

The position $z = 0$ is mid-way between the two ends of the capillary.

Figure 12 shows the component partial pressure profiles, along the distance of the 200 nm capillary tube. These profiles are for time, t = 10 h from the start. The overshoot, and undershoot in the partial pressure of nitrogen is evident.

7. Description of Tuchlenski, Yang, and Veldsink experiments

Figure 13 presents a schematic showing the two-compartment membrane set-up used in the dynamic experiments reported by Tuchlenski et al.,[9] Yang et al.,[27] and Veldsink et al.[28] The two compartments are separated by a porous membrane. The Tuchlenski and Yang experiments are for a mesoporous Vycor glass membrane; the average pore size of the membrane has values in the range 3.8 to 4.7 nm (data from Table 1of Tuchlenski paper). The Veldsink experiments are for an alumina membrane with an average pore diameter $\approx$ 100 nm (see page 285 of Veldsink paper). The physical characteristics of the membranes, determined from fitting of noble gas permeation experiments, are summarized in Table 2, Table 3, and Table 4, for the Tuchlenski, Yang, and Veldsink experiments, respectively.

The experiments reported by Tuchlenski, Yang, and Veldsink are for binary mixtures and are analogous in character. The upstream compartment is maintained at constant composition maintaining a through-flow of the gas mixture at constant composition (a stirrer device is also used in the Veldsink experiments). The feed to the upstream compartment occurs at such a rate as to maintain constant compositions in the upstream compartment that correspond to the inlet feed composition. The total

system pressure in the upstream compartment is 10^5 Pa. The downstream compartment is closed, and is initially maintained at $p_{t0} = 10^5$ Pa.

In order to elucidate the experiments, let us consider the experimental data reported by Tuchlenski et al.,[9] for He-Ar mixtures at 293 K; their experimental data are indicated by the symbols in Figure 14. For each mixture, two sets of experiments were performed. In the first set of experiments, the downstream compartment is initially filled with pure Ar, and the upstream compartment is fed with pure He. Initially, the total system pressure in the downstream compartment is $p_{t0} = 10^5$ Pa. Due to rapid diffusion of He into the downstream compartment, the total pressure, p_t, in the downstream compartment increases in magnitude. This pressure increase is measured and are indicated in Figure 14 by circles. The plotted data are for $(p_t - p_{t0})$. The system will evolve to a steady state wherein the total downstream pressure will equilibrate to 10^5 Pa, corresponding also the total system pressure in the upstream compartment.

In the second experiment, the compositions in the upstream and downstream compartments are reversed. Initially, the downstream compartment contains pure He and the upstream compartment is fed with pure Ar. The rapid efflux of He from the downstream compartment, with concomitant influx of Ar, results in a decrease in the downstream pressure, p_t; the experimental data are shown by the square symbols in Figure 14.

A differential balance over the "closed" downstream compartment (volume = $V_{compartment}$) results in

$$V_{compartment}\frac{1}{RT}\frac{\partial p_t(t)}{\partial t} = A_{membrane}(N_1(t) + N_2(t)) \tag{37}$$

The solution to the set of equations (5) and (37) need to be carried out numerically, as explained by Veldsink et al.[28] and Tuchlenski et al.[9] The numerical solution procedure is simplified by using the linearization technique suggested by Krishna,[13] as explained below.

In our simulations, the "hold-up" of either component within the membrane layer due to any species adsorption is neglected. This assumption is justified for the following reasons. In Table 5 we present the calculations of the total volume of the pores to that of the downstream compartment; the value

$\frac{V_{pore}}{V_{compartment}} = 1.7 \times 10^{-3}$ for the Tuchlenski and Yang experiments. Therefore, the hold-up within the pores of the membrane can be neglected without loss of accuracy.

For adsorbing species *i*, we adjust the value of $Đ_i$ to be a fraction of the value of the corresponding value of the Knudsen diffusivity $D_{i,Kn}$, calculated from equation (4). To be consistent with the M-S formulation, we do not account for viscous flow effects; any such effects are subsumed into the values of chosen values of $Đ_i$. It must be pointed out that for the Vycor glass membrane, viscous flow effects are of negligible importance. For the macroporous membrane used in the Veldsink experiments, the viscous flow effects are non-negligible, but small.

The "linearization" procedure essentially involves the assumption that the matrix [*B*], defined in equation (9) for DGM and by equation (27) for the M-S model, can be considered to be constant during the discretized time interval, provided it is evaluated at the average compositions $\bar{x}_1$ and $\bar{x}_2$ within the membrane, of thickness δ, for the duration of the discretized time interval for integration of equation (37). Essentially, the linearization procedure allows the explicit evaluation of the fluxes for the discretized time interval. The linearized model results in the following expression at time *t*

$$\begin{pmatrix} N_1(t) \\ N_2(t) \end{pmatrix} = \frac{1}{RT} \frac{[B]^{-1}}{\delta} \begin{pmatrix} \left(p_{10} - p_{1\delta}(t)\right) + \overline{x}_1(t)\left(\frac{B_0 p_{t\delta}(t)}{\eta D_{1,Kn}} + 1\right)\left(p_0 - p_{t\delta}(t)\right) \\ \left(p_{20} - p_{2\delta}(t)\right) + \overline{x}_2(t)\left(\frac{B_0 p_{t\delta}(t)}{\eta D_{2,Kn}} + 1\right)\left(p_0 - p_{t\delta}(t)\right) \end{pmatrix} \tag{38}$$

For the M-S model, the viscous flow contribution in the second right member of equation (38) is neglected.

Veldsink et al.[28] provides a comparison of the linearized procedure for calculation of the fluxes, with the exact solution to the DGM and has reported "remarkable agreement" between the two sets. In view of this finding, for all the simulations of the Veldsink, Tuchlenski, and Yang experiments, reported below, the linearized procedure was implemented in MathCad 15.[29]

From equations (37) and (38), we see that the geometrical parameter $\frac{V_{compartment}\delta}{A_{membrane}}$ is relevant for the dynamic pressure increase. For the simulations of the Tuchlenski, and Yang experiments, the value of $\frac{V_{compartment}\delta}{A_{membrane}}$ used in the simulations were calculated using geometrical details provided in Table 1 of Tuchlenski et al.[9] The detailed calculations are also provided in Table 5. Indeed, $\frac{V_{compartment}\delta}{A_{membrane}}$ is not a fit parameter in our simulations of the Tuchlenski and Yang experiments. These experiments were also simulated by Schlünder et al.[30] but in their simulations the values of $\frac{V_{compartment}\delta}{A_{membrane}}$ were fitted separately for each individual experiment for each experiment.

The input data for the simulations of Tuchlenski, Yang, and Veldsink experiments are conveniently summarized in Table 2, Table 3, and Table 4 in order to enable interested readers to reproduce our calculations.

8. Simulations of transient experiments with poorly adsorbing gases

Let us begin by considering the set of experiments with binary mixture consisting of components that have poor adsorption on the pore surfaces.

Consider first the He(1)-Ar(2) experiments of Tuchlenski for permeation across a Vycor glass membrane with a pore size $d_p \approx 4$ nm; see Figure 14. The viscous flow contributions are small; the term $\frac{B_0 p_t}{\eta}\left(\frac{x_1}{D_{1,Kn}}+\frac{x_2}{D_{2,Kn}}\right)$ indicates the fractional contribution of viscous flow to the changes in the total pressure. The fractional viscous flow contribution to changes in total pressure is negligibly small $\frac{B_0 p_t}{\eta}\left(\frac{x_1}{D_{1,Kn}}+\frac{x_2}{D_{2,Kn}}\right)=8.8\times10^{-3}$. The transport fluxes are dominated by molecule-wall interactions, as is evident from the values $\frac{D^e_{1,Kn}}{D^e_{12}}=\frac{D_{1,Kn}}{D_{12}}=0.05$ and $\frac{D^e_{2,Kn}}{D^e_{12}}=\frac{D_{2,Kn}}{D_{12}}=0.016$. The continuous solid lines in

Figure 14 are the solutions to equation (37), in combination with equation (10) obtained from a numerical algorithm implemented in MathCad 15. There is excellent agreement between the experimental data and the DGM model. Similar good agreement is also reported by Tuchlenski et al;[9] see Figure 5 of their paper.

Figure 15 shows the experimental data of Yang et al.[27] for the dynamic pressure increase in the downstream compartment for He(1)-N_2(2) mixtures at 293 K. The viscous flow contributions are small but finite; the term $\frac{B_0 p_t}{\eta}\left(\frac{x_1}{D_{1,Kn}}+\frac{x_2}{D_{2,Kn}}\right)$ indicates the fractional contribution of viscous flow to the changes in the total pressure. The fractional viscous flow contribution to changes in total pressure is $\frac{B_0 p_t}{\eta}\left(\frac{x_1}{D_{1,Kn}}+\frac{x_2}{D_{2,Kn}}\right)=0.165$. The continuous solid lines are the calculations using the DGM model. We note that there is excellent agreement between experiments and simulations, as is to be expected for poorly adsorbing gases.

Consider next the data of Veldsink et al.[28] for He-Ar mixtures; the Veldsink experiments are for an alumina membrane with an average pore size $d_p \approx 100$ nm. The viscous flow contributions are small but finite; the term $\frac{B_0 p_t}{\eta}\left(\frac{x_1}{D_{1,Kn}}+\frac{x_2}{D_{2,Kn}}\right)$ indicates the fractional contribution of viscous flow to the changes in the total pressure. The fractional viscous flow contribution to changes in total pressure is $\frac{B_0 p_t}{\eta}\left(\frac{x_1}{D_{1,Kn}}+\frac{x_2}{D_{2,Kn}}\right)=0.098$. The transport fluxes are dictated by both molecule-wall and molecule-molecule interactions, as is evident from the values $\frac{D^e_{1,Kn}}{D^e_{12}}=0.916$ and $\frac{D^e_{2,Kn}}{D^e_{12}}=0.29$. The continuous solid lines in Figure 16a are the solutions to equation (37), in combination with equation (10) obtained from a numerical algorithm implemented in MathCad 15. There is excellent agreement between the experimental data and the DGM model. Similar good agreement for He-Ar mixtures is also reported by Veldsink et al.[28]

Figure 16b presents a comparison of the experimental data of Veldsink et al.[28] for He-N_2 mixtures with the solution to the DGM model. The viscous flow contributions are small but finite; the term $\frac{B_0 p_t}{\eta}\left(\frac{x_1}{D_{1,Kn}}+\frac{x_2}{D_{2,Kn}}\right)$ indicates the fractional contribution of viscous flow to the changes in the total pressure. The fractional viscous flow contribution to changes in total pressure is $\frac{B_0 p_t}{\eta}\left(\frac{x_1}{D_{1,Kn}}+\frac{x_2}{D_{2,Kn}}\right)=0.108$. The transport fluxes are dictated by both molecule-wall and molecule-molecule interactions, as is evident from the values $\frac{D^e_{1,Kn}}{D^e_{12}}=0.946$ and $\frac{D^e_{2,Kn}}{D^e_{12}}=0.358$. Again, excellent agreement between the DGM model and experiments is realized, in agreement with the findings of Veldsink et al.[28]

9. Transient overshoots/undershoots for mixture uptake within adsorbent particles

Overshoots, and undershoots are also possible for mixture diffusion inside mesoporous and macroporous particles. In order to demonstrate this, we perform simulations for uptake of binary He-Armixtures inside a spherical mesoporous adsorbent particle.

For transient unary uptake within a spherical particle of radius r_c, the radial distribution of pore concentrations, c_i, is obtained from a solution of a set of differential equations describing the uptake

$$\varepsilon\frac{\partial c_i(r,t)}{\partial t}=-\frac{1}{r^2}\frac{\partial}{\partial r}\left(r^2 N_i\right) \tag{39}$$

At any time t, during the transient approach to thermodynamic equilibrium, the spatially averaged molar concentration within the adsorbent particle of radius r_c is obtained by integration of the radial loading profile

$$\bar{c}_i(t)=\frac{3}{r_c^3}\int_0^{r_c} c_i(r,t)r^2 dr \tag{40}$$

An analytical solution to equation (39) is only possible for the special case in which the matrix [B], defined by equation (9) can be considered constant for the range of concentrations encountered within the particle.

Let us consider a particle that has the uniform concentration (c_0). At time $t = 0$, the external surface is brought into contact with a mixture of composition ($c_{r=rc}$). The surface concentration ($c_{r=rc}$) is maintained for the entire duration of the equilibration process. The expression for fractional approach departure from equilibrium is given by the 2-dimensional matrix equation

$$\left(\bar{c}(t) - c_{r=rc}\right) = [Q](c_0 - c_{r=rc}); \quad [Q] \equiv \frac{6}{\pi^2}\sum_{m=1}^{\infty}\frac{1}{m^2}\exp\left[-m^2\pi^2\frac{[B]^{-1}t}{r_c^2}\right] \tag{41}$$

The matrix [Q] quantifies the departure from equilibrium. The Sylvester theorem, detailed in Appendix A of Taylor and Krishna,[31] is required for explicit calculation of the composition trajectories described by Equation (41).

Figure 17 shows the simulations for transient uptake of He-Ar mixtures in a spherical adsorbent particle of radius 2 mm. The chosen temperature of operation is 293 K, and the structural parameters used to calculate the intra-particle diffusivities are the same as those used to model the Tuchlenski experiments; these are specified in Table **2**. Initially, the partial pressures of He, and Ar are p_{10} = 0 kPa, p_{20} = 100 kPa, respectively. At time $t = 0$, the external surface is maintained at $p_{1,eq}$ = 100 kPa, $p_{2,eq}$ = 0 kPa. The time-evolution of the partial pressures, and total pressures are shown.

There is an overshoot in the total pressure, due to rapid influx of the more mobile helium inside the pores of the particle.

Pressure overshoots are also observed for transient uptake inside particle made of mesoporous Vycor glass exposed to a gas phase He(1)/N_2(2) mixture at 293 K. The structural information about Vycor glass has been taken from Yang et al.[27] The average pore diameter is 4 nm. For mesoporous particles, there is a core region in which the molecules do not experience any interactions with the pore wall. The molecule-molecule interactions are described by the bulk gas phase diffusivity for He-N_2 mixtures at 293 K, that can be calculated from the FSG method: $D_{12} = 7.168\times10^{-5}$ m^2 s^{-1}. We performed uptake

simulations for a spherical particle made of radius = 2 mm, in which the particle is first equilibrated with partial pressures are p_1 = 0 kPa; p_2 = 100 kPa, For times, $t \geq 0$, the partial pressures of the components in the bulk gas phase are maintained at p_1 = 100 kPa; p_2 = 0. This implies that there is influx of the more mobile He molecules and efflux of the tardier N_2. Due to the more rapid influx of He, there is an overshoot in the total pressure, $p_t = p_1 + p_2$, during the earlier transience; see Figure 18.

Pressure overshoots within mesoporous catalysts are not uncommon; see Jackson[32] for detailed discussions.

10. Simulations of Tuchlenski experiments with adsorbing gases

Tuchlenski et al.[9] report experimental data for dynamic pressure changes during permeation of He-CO_2, and He-C_3H_8 mixtures at 293 K, at 343 K. Their experimental data are shown by the circle and square symbols in Figure 19, and Figure 20. The simulations using the DGM equation (5) do not yield good agreement with the He-CO_2 and He-C_3H_8 experimental data. Tuchlenski et al.[9] properly recognize that the deviations are due to finite adsorption on the pore walls of CO_2, and C_3H_8. In the DGM concept (see Figure 1), surface diffusion is an additive and parallel contribution to the component fluxes. Tuchlenski et al.[9] have modelled the dynamic permeation experiments by means of a surface diffusion model developed by Krishna.[7, 8] In Table 5 of the Tuchlenski paper, values of surface diffusivities of CO_2, and C_3H_8 are reported for 293 K, at 343 K; these values may be regarded as "fitted parameters". The fitted values of the surface diffusivities have values in the range 2.2 to 4×10^{-9} m^2 s^{-1}.

We adopt a different approach to simulating the Tuchlenski experiments, using the Maxwell-Stefan Equation (22), as applied to mesoporous materials.[15-18] Using MD simulations for a wide variety of unary and binary systems in pores ranging from 2 nm to 20 nm in size,[15-19, 21-23, 33-36] we anticipate that the M-S diffusivity $Đ_i$ to be lower than the corresponding Knudsen diffusivity $D_{i,Kn}$ by a factor that depends on the adsorption strength.

Tuchlenski et al.[9] have also measured the adsorption isotherm for CO_2 and C_3H_8 at 293 K and 343 K; see Table 2 of their paper for the Langmuir adsorption constants. Based on the adsorption isotherms we

note that CO_2 has stronger adsorption strength that C_3H_8. We should therefore expect that the following hierarchy of M-S diffusivities: $Đ_{CO2} < Đ_{C3H8}$. Since the adsorption strength decreases with increasing temperature, we should also expect $Đ_{CO2,293K} < Đ_{CO2,343K}$, and $Đ_{C3H8,293K} < Đ_{C3H8,343K}$.

In applying the M-S equations to model the Tuchlenski experiments in Figure 19, and Figure 20, there are only two adjustable parameters, viz. $Đ_{CO2}$, and $Đ_{C3H8}$.

For the He-CO_2 mixture permeation data at 293 K, and 343 K shown in Figure 19, reasonably good match with experiments are obtained by taking $Đ_{CO2} = 0.55 D_{CO2,Kn}$ for 293 K data, and $Đ_{CO2} = 0.7 D_{CO2,Kn}$ for 343 K data. The higher value of $Đ_{CO2}$ at 343 K is because the adsorption strength is lower at the higher temperature.

For the He-C_3H_8 mixture permeation data at 293 K, and 343 K in Figure 20, reasonably good match with experiments are obtained by taking $Đ_{C3H8} = 0.78 D_{C3H8,Kn}$ for 293 K data, and $Đ_{C3H8} = 0.87 D_{C3H8,Kn}$ for 343 K data. The higher value of $Đ_{C3H8}$ at 343 K is because the adsorption strength is lower at the higher temperature.

Tuchlenski et al.[9] have also published experimental data for CO_2-C_3H_8 mixtures at 293 K; see Figure 21. The two set of experiments are for switching pure CO_2 with 1:1 CO_2/C_3H_8 mixture and vice versa. In this case, the DGM equation (5) predicts a pressure increase close to zero because the values of the Knudsen diffusivities for both CO_2, and C_3H_8 are almost identical because of their near-equal molar masses. This is also evident from Equation (8) for equimolar counter-diffusion; if both Knudsen diffusivities are identical, the total flux N_t, calculated from the DGM neglecting surface diffusion, and there is no change in the total system pressure, p_t.

The experimental data in Figure 21 provide us with an opportunity to test the predictive capability of the M-S formulation because the values $Đ_{CO2} = 0.55 D_{CO2,Kn}$, and $Đ_{C3H8} = 0.78 D_{C3H8,Kn}$ at 293 K have already available from the earlier fits. The dashed lines in Figure 21 are the calculations from the M-S model using these input data values. The agreement between the simulations and experimental data is remarkably good and confirms the predictive capability of the M-S theory.

The M-S model calculations are extremely sensitive to the choice of the values of the M-S diffusivities $Đ_{CO2}$, and $Đ_{C3H8}$. In order to demonstrate this, we compare the experimental data with different scenarios for $Đ_{CO2}$, while maintaining the value $Đ_{C3H8} = 0.78 D_{C3H8,Kn}$. For the experiment in which the downstream compartment is pure CO_2, and the upstream compartment contains a 1:1 CO_2/C_3H_8 mixture of constant composition, the M-S model calculations taking $Đ_{CO2}$ as a factor 1.0, 0.78, 0.55, and 0.45 times the Knudsen value are shown in Figure 22. For the choice $Đ_{CO2} = 1.0 D_{CO2,Kn}$, the model predicts a decrease in the downstream compartment pressure, because C_3H_8 is the tardier component in this scenario. The choice $Đ_{CO2} = 0.78 D_{CO2,Kn}$ anticipates no increase or decrease in the total pressure, because the mobilities of both guest species are the same. In other words, the changes in the downstream pressure are linked to differences in the mobilities of the guest molecules. The choice $Đ_{CO2} = 0.45 D_{CO2,Kn}$ predicts a significantly larger increase in the downstream pressure than observed in the experiments.

In order to elucidate the differences in the DGM model neglecting surface diffusion and the M-S model with adjusted values of $Đ_{CO2}$, and $Đ_{C3H8}$, Figure 23a provides a comparison of the transmembrane fluxes calculated by the DGM (continuous solid lines) and Maxwell-Stefan (dashed lines) models for the Tuchlenski experiments for CO_2-C_3H_8 mixtures at 293 K in which the downstream compartment is initially filled with CO_2, and the upstream compartment is maintained at constant composition with a 1:1 CO_2-C_3H_8 mixture at 10^5 Pa. Since the Knudsen diffusivities of $D_{CO2,Kn}$, and $D_{C3H8,Kn}$ are almost identical, the transmembrane fluxes sum to zero, $N_1 + N_2 = N_t \approx 0$; this follows directly from Equation (8). Due to stronger adsorption of CO_2, this component moves more tardily within the pores. This implies that CO_2 vacates the downstream compartment less quickly than the influx of C_3H_8 from the left compartment. The net result is a positive total flux $N_1 + N_2 = N_t > 0$ directed into the downstream compartment; see the dashed lines in Figure 23a; this net flux results in a pressure increase during transient equilibration.

Figure 23b shows the calculations of the component permeances Π_i using the DGM and M-S model calculations

$$\Pi_i = \frac{N_i}{p_{i0} - p_{i\delta}(t)} \tag{42}$$

From DGM calculations, the permeances of CO_2 and C_3H_8 are indistinguishable from each other because of the use of the Knudsen prescriptions. The M-S model calculations, on the other hand, show the permeance of CO_2 is lower than that of C_3H_8 by about 25% to 45%.

Our analysis of the Tuchlenski experiments with the M-S model leads to the conclusion that the permeance of CO_2 should indeed be lower than that of C_3H_8 due to its stronger adsorption.

11. Simulations of Yang experiments with adsorbing gases

Figure 24 presents a comparison of experimental data of Yang et al.[27] for the dynamic pressure increase in the downstream compartment for He-CO_2 mixtures at 293 K with model calculations. The continuous solid lines are the calculations using the DGM equation (5). The dashed lines are the calculations using the M-S equation (25), taking $Đ_{He} = D_{He,Kn}$ and $Đ_{CO2} = 0.55 D_{CO2,Kn}$. These results are analogous to those presented in Figure 19 for analysis of Tuchlenski data. The adjusted M-S diffusivity of CO_2 for use in the modelling of the Yang experiments is nearly the same as those used to model the Tuchlenski experiments. The M-S diffusivity of CO_2 is lowered below the corresponding Knudsen prescription because of strong adsorption on the pore walls.

Figure 25 compares the experimental data of Yang et al.[27] for the dynamic pressure increase in the downstream compartment for CO_2-C_3H_8 mixtures at 293 K with the DGM and M-S models. The two sets of experiments are for switching pure CO_2 with pure C_3H_8, and vice versa. The continuous solid lines are the calculations using the DGM equation (5). In this case, the DGM equation (5) predicts a pressure increase close to zero because the values of the Knudsen diffusivities for both CO_2, and C_3H_8 are almost identical because of their near-equal molar masses. This is also evident from Equation (8); if

both Knudsen diffusivities are identical, the total flux N_t, calculated from the DGM neglecting surface diffusion, and there is no change in the total system pressure, p_t.

The dashed lines are the calculations using the M-S equation (25), taking $Đ_{CO2} = 0.55 D_{CO2,Kn}$ and $Đ_{C3H8} = 0.88 D_{C3H8,Kn}$. These results are entirely analogous to those presented in Figure 21 for the Tuchlenski data analysis.

In order to explain the differences in the DGM model, neglecting surface diffusion, and the M-S model with adjusted values of $Đ_{CO2}$, and $Đ_{C3H8}$, Figure 26a provides a comparison of the transmembrane fluxes calculated by the DGM (continuous solid lines) and Maxwell-Stefan (dashed lines) models for the Yang experiments for CO_2-C_3H_8 mixtures at 293 K in which the downstream compartment is initially filled with CO_2, and the upstream compartment is flushed with pure C_3H_8 at 10^5 Pa. Since the Knudsen diffusivities of $D_{CO2,Kn}$, and $D_{C3H8,Kn}$ are almost identical, the transmembrane fluxes sum to zero, $N_1 + N_2 = N_t \approx 0$; this follows directly from Equation (8). Due to stronger adsorption of CO_2, this component moves more tardily within the pores. This implies that CO_2 vacates the downstream compartment less quickly than the influx of C_3H_8 from the left compartment. The net result is a positive total flux $N_1 + N_2 = N_t > 0$ directed into the downstream compartment; see the dashed lines in Figure 26a; this net flux results in a pressure increase during transient equilibration.

Figure 26b shows the calculations of the component permeances Π_i using the DGM and M-S model calculations. From DGM calculations, the permeances of CO_2 and C_3H_8 are indistinguishable from each other because of the use of the Knudsen prescriptions. The M-S model calculations, on the other hand, show the permeance of CO_2 is lower than that of C_3H_8 by about 25% to 45%.

Our analysis of the Yang experiments with the M-S model leads to the conclusion that the permeance of CO_2 should indeed be lower than that of C_3H_8 due to its stronger adsorption.

12. Ratio of M-S diffusivity to Knudsen diffusivity plotted as a function of Henry coefficient for adsorption

Figure 27 presents a plot of the ratio, $Đ_i/D_{i,Kn}$, determined as explained in the foregoing analysis of both Tuchlenski and Yang experiments, plotted as a function of the Henry coefficient for adsorption. This plot, which is entirely analogous that that derived from MD simulations in Figure 6; this confirms that the lowering in the M-S diffusivity below the Knudsen prescription increases with increasing adsorption strength. The information contained in this graph, provides an engineering approach to the estimation of the M-S diffusivity $Đ_i$ by using the Knudsen diffusivity $D_{i,Kn}$ as a pivotal value for that species.

We list below further experimental data in the literature that strengthen the findings in Figure 6.

In the work of Tsuru et al.[37], the experimentally determined permeance of strongly adsorbing H_2O molecules across silica membranes, is significantly lower than anticipated on the basis of its molecular size. This is most likely due to the strong adsorption of H_2O molecules on the pore walls, causing violation of the Knudsen prescription.

In the experimental study of Katsanos et al.[38], the ratio $Đ_i/D_{i,Kn}$ for diffusion of nC5, nC6 and nC7 in α-alumina (d_p = 21.6 nm) and γ-alumina (d_p = 10.6 nm) were found to be in the range of 0.1 – 0.27.

Further experimental evidence on departure from the Knudsen prescription is provided by the experimental data reported by Petukhov and Eliseev[39] on the permeances of CO_2, and C_3H_8 across an alumina membrane with an average pore diameter d_p = 45 nm. Their data show that permeance of CO_2 is about 90% lower than that of C_3H_8. From equation (28), $\Pi_i = (\varepsilon/\tau)Đ_i/RT\delta$ for the scenario in which molecule-wall collisions dominate. The data of Petukhov indicate that $Đ_{CO2} \approx 0.9Đ_{C3H8}$, at variance with the expectations from equation (4).

13. Simulations of Veldsink experiments with adsorbing gases

Veldsink et al.[28] report experimental data on the dynamic pressure changes for He-CO_2 mixtures at 293 K, and at 434 K; see Figure 28a, and Figure 28b. Good agreement is obtained with the M-S

formulation taking $Đ_{CO2} = 0.85 D_{CO2,Kn}$ at 293 K and and $Đ_{CO2} = 0.9 D_{CO2,Kn}$ at 434 K. The fitted values are somewhat higher than the corresponding values obtained for fitting the corresponding Tuchlenski data (see Figure 19). The reason is that the pore size of the membrane in the Veldsink experiments is 100 nm, considerably larger than the 4 nm pore sized membrane used in the Tuchlenski and Yang experiments. The larger the pore size, the closer is the approach of the M-S diffusivity $Đ_{CO2}$ to the Knudsen limit; this is in conformity with MD simulation data reported in the literature. [15-19, 21-23, 33-36]

The experimental data of Veldsink et al.[28] for He-C_3H_8 mixtures at 293 K, and 416 K are shown in Figure 29. These data can be matched well by taking $Đ_{C3H8} = 0.95 D_{C3H8,Kn}$ at 293 K and $Đ_{C3H8} = 0.98 D_{C3H8,Kn}$ at 416 K. These M-S diffusivity values are higher than the corresponding values for CO_2 (see Figure 28) because of the lower adsorption strength of C_3H_8.

14. Comparison of Tuchlenski CO_2/C_3H_8 experiments with surface diffusion model

In the foregoing analysis of Tuchlenski experiments with CO_2-C_3H_8 mixtures, no explicit account was taken of surface diffusion. The model calculations were based on the assumption that the influence of adsorption on the pore walls is to introduce a bias into the hops, and reduce the M-S diffusivities $Đ_{CO2}$, and $Đ_{C3H8}$ below those prescribed by the Knudsen formula.

A different modelling approach is to assume that the mechanism of transport of both CO_2, and C_3H_8 is exclusively by diffusion along the surface. Since molecule-molecule interactions are of negligible importance, the component fluxes are described by equation (11).

In 2-dimensional matrix, the flux relations are

$$\begin{pmatrix} N_1(t) \\ N_2(t) \end{pmatrix} = \frac{(\varepsilon/\tau)}{\delta} \begin{bmatrix} Đ_{1,s} & 0 \\ 0 & Đ_{2,s} \end{bmatrix} \begin{bmatrix} \Gamma_{11} & \Gamma_{12} \\ \Gamma_{21} & \Gamma_{22} \end{bmatrix} \begin{pmatrix} c_{10} - c_{1\delta}(t) \\ c_{20} - c_{2\delta}(t) \end{pmatrix} \tag{43}$$

Equation (43) is used in place of equation (38) for calculation of the fluxes. The driving forces are the differences in the molar concentrations in the pore at the upstream face (c_{i0}, maintained constant) and

the downstream face of the membrane, ($c_{i\delta}(t)$, varying with time). The pore concentrations are calculated using mixed-gas Langmuir model

$$\frac{c_1}{c_{1,sat}} = \theta_1 = \frac{b_1 p_1}{1 + b_1 p_1 + b_2 p_2}; \quad \frac{c_2}{c_{2,sat}} = \theta_2 = \frac{b_2 p_2}{1 + b_1 p_1 + b_2 p_2} \tag{44}$$

using the partial pressures p_{i0}, and $p_{i\delta}(t)$.

For the mixed-gas Langmuir model, equation (44), we can derive simple analytic expressions for the four elements of the matrix of thermodynamic factors:[40]

$$\begin{bmatrix} \Gamma_{11} & \Gamma_{12} \\ \Gamma_{21} & \Gamma_{22} \end{bmatrix} = \frac{1}{1 - \theta_1 - \theta_2} \begin{bmatrix} 1 - \theta_2 & \frac{c_{1,sat}}{c_{2,sat}} \theta_1 \\ \frac{c_{2,sat}}{c_{1,sat}} \theta_2 & 1 - \theta_1 \end{bmatrix} \tag{45}$$

The Langmuir parameters are provided in Table 2 of Tuchlenski et al.[9] To retain thermodynamic consistency, we use the Langmuir fit parameters in which the component saturation capacities of CO_2, and C_3H_8 are identical.

We now attempt to try to determine the surface diffusivities, $Đ_{i,s}$, of CO_2, and C_3H_8 by matching with experimental data. For this purpose, we assume that the surface diffusivities are independent of pore concentrations. A reasonably good match of the experimental data of Tuchlenski et al.[9] is obtained by taking the values of the M-S surface diffusivities $Đ_{CO2,s} = 0.5 D_{CO2,Kn}$, and $Đ_{C3H8,s} = 0.85 D_{C3H8,Kn}$; see the simulation results indicated by the continuous solid lines in Figure 30. The calculations of the surface diffusion model are in fair agreement with the "mesopore diffusion" model in which the M-S diffusivities for hopping along the pore walls was taken as $Đ_{CO2} = 0.55 D_{CO2,Kn}$, and $Đ_{C3H8} = 0.78 D_{C3H8,Kn}$; these results were discussed earlier in the context of Figure 21. Remarkably, the use of the surface diffusion model also leads to the conclusion that the M-S surface diffusivities are lowered below the Knudsen prescription, by approximately the same factor as determined from the "mesopore diffusion" model.

Implicit in the results presented in Figure 30 is that the surface diffusion should not be viewed as an additional contribution to the fluxes as is suggested by schematic in Figure 1 that was put forward by Mason and Malinauskas.[1]

15. Comparison of Yang CO_2/C_3H_8 experiments with surface diffusion model

In the foregoing analysis of Yang experiments with CO_2-C_3H_8 mixtures, no explicit account was taken of surface diffusion. The model calculations were based on the assumption that the influence of adsorption on the pore walls is to introduce a bias into the hops, and reduce the M-S diffusivities $Đ_{CO2}$, and $Đ_{C3H8}$ below those prescribed by the Knudsen formula.

We now attempt to model the Yang experiments for CO_2-C_3H_8 mixtures using the surface diffusion model, described in an earlier section. The Langmuir parameters are provided in Table 1 of Yang et al.[27] To retain thermodynamic consistency we use the Langmuir fit parameters in which the component saturation capacities of CO_2, and C_3H_8 are identical.

We now attempt to try to determine the surface diffusivities, $Đ_{i,s}$, of CO_2, and C_3H_8 by matching with experimental data. For this purpose, we assume that the surface diffusivities are independent of pore concentrations. A reasonably good match of the experimental data presented in Figure 6 of Yang et al.[27] is obtained by taking the values of the M-S surface diffusivities $Đ_{CO2,s} = 0.35 D_{CO2,Kn}$, and $Đ_{C3H8,s} = 0.85 D_{C3H8,Kn}$; see the simulation results indicated by the continuous solid lines in Figure 31.

The calculations of the surface diffusion model are in fair agreement with the "mesopore diffusion" model in which the M-S diffusivities for hopping along the pore walls was taken as $Đ_{CO2} = 0.55 D_{CO2,Kn}$, and $Đ_{C3H8} = 0.88 D_{C3H8,Kn}$; these results were discussed earlier in the context of Figure 25. Remarkably, the use of the surface diffusion model also leads to the conclusion that the M-S surface diffusivities are lowered below the Knudsen prescription, by approximately the same factor as determined from the "mesopore diffusion" model.

In Figure 7 of Yang et al,[27] experimental data are presented for dynamic pressure increases in the downstream compartment for varying compositions. For the experiments in which 3:7 CO_2-C_3H_8 mixture in the downstream compartment is displaced by 1:9 CO_2-C_3H_8 in the upstream compartment, and vice versa, the experimental data on transient pressure changes are properly captured by the surface diffusion model using the same set of values of the M-S surface diffusivities $Đ_{CO2,s} = 0.35 D_{CO2,Kn}$, and $Đ_{C3H8,s} = 0.85 D_{C3H8,Kn}$ as used earlier (in the other set of experiments discussed earlier in Figure 31); see comparisons of simulations with experiment in Figure 32.

16. Notation

$A_{membrane}$	cross-sectional area of membrane, m^2
B_0	permeability of pore, m^2
$[B]$	matrix defined by equation (9) for DGM and (27) for M-S model, m^{-2} s
c_i	molar concentration of species *i*, mol m^{-3}
$c_{i,sat}$	molar concentration of adsorbed species *i* at saturation, mol m^{-3}
c_t	total molar concentration of mixture, mol m^{-3}
d_p	diameter of pore, m
$Đ_i$	M-S diffusivity for molecule-wall interaction, m^2 s^{-1}
$Đ_{i,s}$	M-S diffusivity for surface diffusion, m^2 s^{-1}
$D_{i,Kn}$	Knudsen diffusivity of species *i*, m^2 s^{-1}
$Đ_{ij}$	Maxwell-Stefan diffusivity for *i-j* pair, m^2 s^{-1}
K_0	effective pore size, also called Knudsen number, m
n	number of species in the mixture, dimensionless
N_i	molar flux of species *i* with respect to framework, mol m^{-2} s^{-1}
p_i	partial pressure of species *i* in mixture, Pa
p_t	total system pressure, Pa
r_c	radius of adsorbent particle, m
R	gas constant, 8.314 J mol^{-1} K^{-1}
u_i	velocity of motion of species *i* with respect to pore wall, m s^{-1}
$V_{compartment}$	volume of downstream compartment, m^3
V_p	pore volume, m^3 kg^{-1}
x_i	mole fraction of species *i* within pore, dimensionless
T	absolute temperature, K
z	distance coordinate, m

Greek letters

δ	thickness of membrane, m
ε	pore voidage, dimensionless
Γ_{ij}	thermodynamic factors, dimensionless
$[\Gamma]$	matrix of thermodynamic factors, dimensionless
μ_i	molar chemical potential of component *i*, J mol^{-1}
Π_i	permeance of species *i* in mixture mol m^{-2} s^{-1} Pa^{-1}
η	viscosity of gas mixture, Pa s
θ_i	fractional occupancy of component *i*, dimensionless
ρ	framework density, kg m^{-3}
σ	Lennard-Jones size parameter, m
τ	tortuosity, dimensionless

Subscripts

i	referring to component *i*
t	referring to total mixture

Superscripts

e	effective parameter inside pore

Table S1. Input data for simulation of Tuchlenski et al.[9] experiments for unary CO_2 permeation. These data are taken from Tables 2, 3 and 5 of Tuchlenski et al.[9] The viscosity data taken from the paper by Veldsink et al.[28]

Porosity/Tortuosity: $\frac{\varepsilon}{\tau} = 0.03$;

$K_0 = \frac{d_p}{4}\frac{\varepsilon}{\tau} = 6.58 \times 10^{-11}$ m;

Permeability: $B_0^e = \frac{d_p^2}{32}\frac{\varepsilon}{\tau} = 10.8 \times 10^{-20}$ m^2;

$A_{membrane} = 2.796 \times 10^{-3}$ m^2; Transfer area from upstream to downstream comparments.

Membrane thickness, $\delta = 1.1 \times 10^{-3}$ m;

Gas phase viscosities:

CO_2 at 293 K: $\eta = 1.73 \times 10^{-5}$ Pa s;

CO_2 at 343 K: $\eta = 2.33 \times 10^{-5}$ Pa s;

The surface diffusivities are from Table 5 of Tuchlenski et al.[9]

CO_2 at 293 K: $Đ_{i,s} = 2.2 \times 10^{-9}$ m^2 s^{-1};

CO_2 at 343 K: $Đ_{i,s} = 2.8 \times 10^{-9}$ m^2 s^{-1};

Please note that the isotherm data reported by Tuchlenski use c_i defined in terms of mol of species *i* per m^3 of solid material.

Table S2. Input data for simulation of Tuchlenski et al.[9] experiments. These data are taken from Tables 1, 2 and 3 of Tuchlenski et al.[9] The viscosity data taken from the paper by Veldsink et al.[28]

Porosity/Tortuosity: $\frac{\varepsilon}{\tau} = 0.03$;

$K_0 = \frac{d_p}{4}\frac{\varepsilon}{\tau} = 6.58\times10^{-11}$ m;

Permeability: $B_0^e = \frac{d_p^2}{32}\frac{\varepsilon}{\tau} = 10.8\times10^{-20}$ m^2;

$\frac{V_{compartment}\delta}{A_{membrane}} = 4\times10^{-6}$ m^2;

1-site Langmuir parameters for CO_2 and C_3H_8 in Vycor glass. From Table 2 of Tuchlenski.

	q_{sat} mol kg^{-1}	b Pa^{-1}
CO_2	1.35	6.01×10^{-6}
C_3H_8	1.35	2.87×10^{-6}

Bulk gas phase diffusivities, and gas phase viscosities:

He-Ar at 293 K: $D_{12} = 7.34\times10^{-5}$ m^2 s^{-1}; $\eta = 2.32\times10^{-5}$ Pa s;

He-CO_2 at 293 K: $D_{12} = 5.792\times10^{-5}$ m^2 s^{-1}; $\eta = 1.73\times10^{-5}$ Pa s;

He-CO_2 at 343 K: $D_{12} = 7.541\times10^{-5}$ m^2 s^{-1}; $\eta = 2.33\times10^{-5}$ Pa s;

He-C_3H_8 at 293 K: $D_{12} = 4\times10^{-5}$ m^2 s^{-1}; $\eta = 1.04\times10^{-5}$ Pa s;

He-C_3H_8 at 343 K: $D_{12} = 5.23\times10^{-5}$ m^2 s^{-1}; $\eta = 1.36\times10^{-5}$ Pa s;

CO_2-C_3H_8 at 293 K: $D_{12} = 9\times10^{-6}$ m^2 s^{-1}; estimated for the Fuller-Schettler-Giddings method.[2, 3]

$\eta = 1.04\times10^{-5}$ Pa s;

Note: All of the above parameters are input data for DGM equation (5). In using the M-S equation (25), the viscous flow contribution is omitted.

Table S3. Input data for simulation of Yang et al.[27] experiments. These data are taken from Tables 1 and 2 of Yang et al.[27] The viscosity data taken from the paper by Veldsink et al.[28]

Porosity/Tortuosity: $\frac{\varepsilon}{\tau} = 0.039$;

$K_0 = \frac{d_p}{4}\frac{\varepsilon}{\tau} = 6.346\times10^{-11}$ m;

Permeability: $B_0^e = \frac{d_p^2}{32}\frac{\varepsilon}{\tau} = 1.748\times10^{-18}$ m^2;

$\frac{V_{compartment}\delta}{A_{membrane}} = 4\times10^{-6}$ m^2;

1-site Langmuir parameters for CO_2 and C_3H_8 in Vycor glass; from Table 1 of Yang.

	q_{sat} mol kg^{-1}	b Pa^{-1}
CO_2	0.8264	8.54×10^{-6}
C_3H_8	0.8264	4.01×10^{-6}

Bulk gas phase diffusivities, and gas phase viscosities:

He-N_2 at 293 K: $D_{12} = 7.168\times10^{-5}$ m^2 s^{-1}; $\eta = 1.83\times10^{-5}$ Pa s;

He-CO_2 at 293 K: $D_{12} = 5.792\times10^{-5}$ m^2 s^{-1}; $\eta = 1.73\times10^{-5}$ Pa s;

CO_2-C_3H_8 at 293 K: $D_{12} = 9\times10^{-6}$ m^2 s^{-1}; estimated for the Fuller-Schettler-Giddings method.[2, 3]

$\eta = 1.04\times10^{-5}$ Pa s;

Note: All of the above parameters are input data for DGM equation (5). In using the M-S equation (25), the viscous flow contribution is omitted.

Table S4. Input data for simulation of Veldsink[28] experiments. These data are taken from Table 5 of Veldsink et al.[28] The viscosity data are taken from the legends to Figures 9, 11, 12, 13, 14, and 15 of Veldsink et al.[28]

Porosity/Tortuosity: $\frac{\varepsilon}{\tau} = 0.08$;

$K_0 = \frac{d_p}{4}\frac{\varepsilon}{\tau} = 3.24 \times 10^{-9}$ m; Pore diameter: $d_p = 0.162$ μm;

Permeability: $B_0^e = \frac{d_p^2}{32}\frac{\varepsilon}{\tau} = 5.89 \times 10^{-17}$ m^2;

$\frac{V_{compartment}\delta}{A_{membrane}} = 5.625 \times 10^{-5}$ m^2;

Bulk gas phase diffusivities, and gas phase viscosities:

He-Ar at 293 K: $D_{12} = 7.34 \times 10^{-5}$ m^2 s^{-1}; $\eta = 2.32 \times 10^{-5}$ Pa s;

He-N_2 at 298 K: $D_{12} = 7.168 \times 10^{-5}$ m^2 s^{-1}; $\eta = 1.83 \times 10^{-5}$ Pa s;

He-CO_2 at 293 K: $D_{12} = 5.792 \times 10^{-5}$ m^2 s^{-1}; $\eta = 1.73 \times 10^{-5}$ Pa s;

He-CO_2 at 434 K: $D_{12} = 11.384 \times 10^{-5}$ m^2 s^{-1}; $\eta = 2.33 \times 10^{-5}$ Pa s;

He-C_3H_8 at 298 K: $D_{12} = 4.158 \times 10^{-5}$ m^2 s^{-1}; $\eta = 1.04 \times 10^{-5}$ Pa s;

He-C_3H_8 at 416 K: $D_{12} = 7.336 \times 10^{-5}$ m^2 s^{-1}; $\eta = 1.36 \times 10^{-5}$ Pa s;

Note: All of the above parameters are input data for DGM equation (5). In using the M-S equation (25), the viscous flow contribution is omitted.

Table S5. Membrane geometry for Tuchlenski and Yang experiments. The geometrical details are taken from Table 1 of Tuchlenski et al.[9]

Inner radius of membrane: $r_1 = 3.9\times10^{-3}$ m;

Outer radius of membrane: $r_2 = 5\times10^{-3}$ m;

Thickness of membrane: $\delta = 1.1\times10^{-3}$ m;

Membrane length: $L = 0.1$ m;

Volume of downstream compartment: $V_{compartment} = 10.4\times10^{-6}$ m^3;

Area of membrane for calculation of fluxes: $A_{membrane} = 2\pi\left(\frac{r_1 + r_2}{2}\right)L = 2.796\times10^{-3}$ m^2;

From above data we calculate: $\frac{V_{compartment}\delta}{A_{membrane}} = 4.1\times10^{-6}$ m^2;

The value used in the simulation of Tuchlenski and Yang experiments: $\frac{V_{compartment}\delta}{A_{membrane}} = 4\times10^{-6}$ m^2;

Porosity of membrane $\varepsilon = 0.284$.

Total volume of pores within membrane layer: $V_{pore} = \pi\left(r_2^2 - r_1^2\right)L\varepsilon = 1.77\times10^{-8}$.

Ratio of total pore volume to downstream compartment volume $\frac{V_{pore}}{V_{compartment}} = 1.7\times10^{-3}$

17. References

(1) Mason, E. A.; Malinauskas, A. P. *Gas Transport in Porous Media: The Dusty-Gas Model*; Elsevier: Amsterdam, 1983.

(2) Fuller, E. N.; Schettler, P. D.; Giddings, J. C. A New Method for Prediction of Binary Gas-phase Diffusion Coefficients. *Ind. Eng. Chem.* **1966**, *58*, 19.

(3) Reid, R.C.; Prausnitz, J. M.; Poling, B. E. *The Properties of Gases and Liquids*; 4th Edition, McGraw-Hill: New York, 1986.

(4) Knudsen, M. Die Gesetze der Molekularströmung und der inneren Reibungsströmung der Gase durch Röhren. *Ann. Phys.* **1909**, *333*, 75.

(5) Smoluchowski, M. Zur Kinetischen Theorie der Transpiration und Diffusion verdünnter Gase. *Ann. Phys.* **1910**, *338*, 1559.

(6) Gruener, S.; Huber, P. Knudsen Diffusion in Dilicon Nanochannels. *Phys. Rev. Lett.* **2008**, *100*, 064502.

(7) Krishna, R. Multicomponent Surface Diffusion of Adsorbed Species - A Description Based on the Generalized Maxwell-Stefan Equations. *Chem. Eng. Sci.* **1990**, *45*, 1779.

(8) Krishna, R. Problems and Pitfalls in the Use of the Fick Formulation for Intraparticle Diffusion. *Chem. Eng. Sci.* **1993**, *48*, 845.

(9) Tuchlenski, A.; Uchytil, P.; Seidel-Morgenstern, A. An Experimental Study of Combined Gas Phase and Surface Diffusion in Porous Glass. *J. Membr. Sci.* **1998**, *140*, 165.

(10) Wu, K.; Li, X.; Wang, C.; Yu, W.; Chen, Z. Model for Surface Diffusion of Adsorbed Gas in Nanopores of Shale Gas Reservoirs. *Ind. Eng. Chem. Res.* **2015**, *54*, 3225.

(11) Young, J. B.; Todd, B. Modelling of Multi-Component Gas Flows in Capillaries and Porous Solids. *Int. J. Heat Mass Transfer* **2005**, *48*, 5338.

(12) Kerkhof, P. J. A. M. A Modified Maxwell-Stefan Model for Transport Through Inert Membranes: The Binary Friction Model. *Chem. Eng. J.* **1996**, *64*, 319.

(13) Krishna, R. A Simplified Procedure for the Solution of the Dusty Gas Model Equations for Steady-State Transport in Non-Reacting Systems. *Chem. Eng. J.* **1987**, *35*, 75.

(14) Remick, R. R.; Geankoplis, C. J. Ternary Diffusion of Gases in Capillaries in the Transition Region Between Knudsen and Molecular Diffusion. *Chem. Eng. Sci.* **1974**, *29*, 1447.

(15) Krishna, R.; van Baten, J. M. An Investigation of the Characteristics of Maxwell-Stefan Diffusivities of Binary Mixtures in Silica Nanopores. *Chem. Eng. Sci.* **2009**, *64*, 870.

(16) Krishna, R.; van Baten, J. M. Unified Maxwell-Stefan Description of Binary Mixture Diffusion in Micro- and Meso- Porous Materials. *Chem. Eng. Sci.* **2009**, *64*, 3159.

(17) Krishna, R. Describing the Diffusion of Guest Molecules inside Porous Structures. *J. Phys. Chem. C* **2009**, *113*, 19756.

(18) Krishna, R. Diffusion in Porous Crystalline Materials. *Chem. Soc. Rev.* **2012**, *41*, 3099.

(19) Krishna, R.; van Baten, J. M. Influence of Adsorption on the Diffusion Selectivity for Mixture Permeation across Mesoporous Membranes. *J. Membr. Sci.* **2011**, *369*, 545.

(20) Krishna, R.; Wesselingh, J. A. The Maxwell-Stefan Approach to Mass Transfer. *Chem. Eng. Sci.* **1997**, *52*, 861.

(21) Bhatia, S. K.; Bonilla, M. R.; Nicholson, D. Molecular Transport in Nanopores: A Theoretical Perspective. *Phys. Chem. Chem. Phys.* **2011**, *13*, 15350.

(22) Krishna, R.; van Baten, J. M. A Molecular Dynamics Investigation of the Unusual Concentration Dependencies of Fick Diffusivities in Silica Mesopores. *Microporous Mesoporous Mater.* **2011**, *138*, 228.

(23) Krishna, R.; van Baten, J. M. Investigating the Validity of the Knudsen Prescription for Diffusivities in a Mesoporous Covalent Organic Framework. *Ind. Eng. Chem. Res.* **2011**, *50*, 7083.

(24) Krishna, R.; van Baten, J. M. Investigating the Validity of the Bosanquet Formula for Estimation of Diffusivities in Mesopores. *Chem. Eng. Sci.* **2012**, *69*, 684.

(25) Duncan, J. B.; Toor, H. L. An Experimental Study of Three Component Gas Diffusion. *A.I.Ch.E.J.* **1962**, *8*, 38.

(26) Krishna, R. Uphill Diffusion in Multicomponent Mixtures. *Chem. Soc. Rev.* **2015**, *44*, 2812.

(27) Yang, J.; Čermáková, J.; Uchytil, P.; Hamel, C.; Seidel-Morgenstern, A. Gas Phase Transport, Adsorption and Surface Diffusion in a Porous Glass Membrane. *Catal. Today* **2005**, *104*, 344.

(28) Veldsink, J. W.; Versteeg, G. F.; Van Swaaij, W. P. M. An Experimental Study of Diffusion and Convection of Multicomponent Gases through Catalytic and Non-Catalytic Membranes. *J. Membr. Sci.* **1994**, *92*, 275.

(29) PTC MathCad 15.0. http://www.ptc.com/, PTC Corporate Headquarters, Needham, 3 November 2015.

(30) Schlünder, E. U.; Yang, J.; Seidel-Morgenstern, A. Competitive Diffusion and Adsorption in Vycor Glass Membranes—A Lumped Parameter Approach. *Catal. Today* **2006**, *118*, 113.

(31) Taylor, R.; Krishna, R. *Multicomponent mass transfer*; John Wiley: New York, 1993.

(32) Jackson, R. *Transport in Porous Catalysts*; Elsevier: Amsterdam, 1977.

(33) Bhatia, S. K.; Nicholson, D. Comments on ‘‘Diffusion in a Mesoporous Silica Membrane: Validity of the Knudsen Diffusion Model’. *Chem. Eng. Sci.* **2010**, *65*, 4519.

(34) Bhatia, S. K.; Jepps, O.; Nicholson, D. Tractable Molecular Theory of Transport of Lennard-Jones Fluids in Nanopores. *J. Chem. Phys.* **2004**, *120*, 4472.

(35) Bhatia, S. K.; Nicholson, D. Transport of Simple Fluids in Nanopores: Theory and Simulation. *A.I.Ch.E.J.* **2006**, *52*, 29.

(36) Bhatia, S. K. Modeling Pure Gas Permeation in Nanoporous Materials and Membranes. *Langmuir* **2010**, *26*, 8373.

(37) Tsuru, T.; Igi, R.; Kanezashi, M.; Yoshioka, T.; Fujisaki, S.; Iwamoto, Y. Permeation Properties of Hydrogen and Water Vapor Through Porous Silica Membranes at High Temperatures. *A.I.Ch.E.J.* **2011**, *57*, 618.

(38) Katsanos, N. A.; Bakaoukas, N.; Koliadima, A.; Karaiskakis, G. Diffusion and Adsorption Measurements in Porous Solids by Inverse Gas Chromatography. *J. Phys. Chem. B* **2005**, *109*, 11240.

(39) Petukhov, D. I.; Eliseev, A. A. Gas Permeation Through Nanoporous Membranes in the Transitional Flow Region. *Nanotechnology* **2016**, *27*, 085707.

(40) Krishna, R.; Baur, R. Modelling Issues in Zeolite Based Separation Processes. *Sep. Purif. Technol.* **2003**, *33*, 213.

18. Caption for Figures

Figure S1. Electric analog circuit picturing the flux of the diffusing species within a porous medium. Adapted from Mason and Malinauskas,[1]

Figure S2. (a) Knudsen ($D_{He,Kn}$, $D_{Ar,Kn}$), and bulk diffusivities ($Đ_{He,Ar}$) of He/Ar mixtures at 293 K in cylindrical mesopores and macropores. The calculations of the bulk diffusivities $Đ_{He,Ar}$ are at total pressures of 0.1 MPa. (b) Influence of total system pressure on the bulk diffusivities $Đ_{He,Ar}$.

Figure S3. (a) Experimental data (shown by symbols) of Remick and Geankoplis[14] for the fluxes of helium (1), neon (2) and argon (3) across a porous capillary diffusion cell made up of cylindrical capillaries of diameter d_p = 39.1 μm, and length δ = 9.6 mm. The fluxes are plotted as a function of the average system pressure. The continuous solid lines are the calculations using the linearized equation (15). The matrix [B] is evaluated at the average composition at either ends of the capilliaries at the average system pressure. (b) Calculations of the fluxes as a function of the capillary diameter, maintaining the total pressure = 10^3 Pa.

Figure S4. Unary CO_2 permeation fluxes across Vycor glass membrane at (a) 293 K, and (b) 343 K with calculations using the combination of the DGM model, both including and neglecting surface diffusion. The input data are provided in Table S1.

Figure S5. (a) MD data on the Maxwell-Stefan diffusivity $Đ_{12}$, for equimolar ($c_1 = c_2$) binary mixture of CH_4-Ar in silica pores with diameters in the range 2 nm to 10 nm. Also shown (square symbols) are the $Đ_{12,fl}$ data for binary fluid CH_4-Ar mixture diffusion, obtained from independent MD simulations. (b, c, d, e) MD data on the Maxwell-Stefan diffusivity for equimolar ($c_1 = c_2$) binary mixtures (b) CO_2- CH_4, (c) CH_4- H_2, (d) CO_2- H_2, and (e) Ar- H_2 in BTP-COF compared with the corresponding values of the $Đ_{12,fl}$ data for binary fluid mixture diffusion, obtained from independent MD simulations. The straight line represents the estimations of the gas phase diffusivity $Đ_{12,fl}$ using the Fuller-Schettler-Giddings method.[2, 3]

Figure S6. (a) MD data of Krishna and van Baten[23] on the M-S diffusivity $Đ_i$ for various guest molecules (hydrogen, argon, carbon dioxide, methane, ethane, propane) in BTP-COF, plotted as function of the pore concentration, c_i. (b) Ratio of the MD data of Krishna and van Baten[23] on the zero-loading diffusivity to the calculated Knudsen diffusivity, $Đ_i(0)/D_{i,Kn}$, for various guest molecules for various guest molecules (H_2, Ar, CH_4, C_2H_6, C_3H_8, nC_4H_{10}, nC_5H_{12}, nC_6H_{14}) in BTP-COF, plotted as function of the Henry coefficient for adsorption of the corresponding species. (c) Ratio of the MD data of Krishna and van Baten[15, 16, 23] on the zero-loading diffusivity to the calculated Knudsen diffusivity, $Đ_i(0)/D_{i,Kn}$, for linear alkanes as a function of C number in BTP-COF, 2 nm cylindrical silica pore, and 3 nm cylindrical pore.

Figure S7. MD data of M-S diffusivity at zero-loading, $Đ_i$, of (a) CH_4, (b) Ar, (c) CO_2, and (c) C_3H_8 in zeolites, MOFs, and silica mesopores, plotted as a function of the pore dimension. The data has been culled from various MD simulation data sources.[15-17]

Figure S8. The two-bulb diffusion experiment of Duncan and Toor[25] with $H_2(1)/N_2(2)/CO_2(3)$ gas mixture.

Figure S9. (a) Experimental data of Duncan and Toor[25] on the transient approach to equilibrium in the two-bulb diffusion experiments for $H_2(1)/N_2(2)/CO_2(3)$ mixtures. (b) Equilibration trajectories in composition space, followed in the two bulbs. The calculations using the Maxwell-Stefan diffusion equations, ignoring molecule-pore wall collisions are shown by the continuous solid lines (for Bulb A) and dashed lines (for Bulb B).

Figure S10. (a) Partial pressures of each component, and (b) total pressure in Bulb A and Bulb B for 200 nm capillary tube joining A and B.

Figure S11. (a) Partial pressures of each component, and (b) total pressure in Bulb A and Bulb B for 2 nm capillary tube joining A and B.

Figure S12. Component partial pressure profiles, along the distance of the 200 nm capillary tube. These profiles are for time, t = 10 h from the start. The position z =0 corresponds to the center point between the two semi-infinite slabs.

Figure S13. Schematic showing the two-compartment membrane set-up used in the experiments reported by Tuchlenski et al.,[9] Yang et al.[27] and Veldsink et al. [28]

Figure S14. Experimental data of Tuchlenski et al.[9] for the dynamic pressure increase in the downstream compartment (data scanned from Figure 5 of Tuchlenski paper) for He-Ar mixtures at 293 K. The continuous solid lines are the calculations using the DGM equation (5). Input data in Table S2.

Figure S15. Experimental data of Yang et al.[27] for the dynamic pressure increase in the downstream compartment (data scanned from Figure 4 of Yang paper) for He-N_2 mixtures at 293 K. The continuous solid lines are the calculations using the DGM equation (5). Input data in Table S3.

Figure S16. Experimental data of Veldsink et al.[28] for the dynamic pressure increase in the downstream compartment(data scanned from Figure 9 and Figure 11 of Veldsink paper) for (a) He-Ar mixtures at 293 K, and (b) He-N_2 mixtures at 298 K. The continuous solid lines are the calculations using the DGM equation (5). Input data in Table S4.

Figure S17. Transient uptake of He-Ar mixtures at 293 K in a spherical adsorbent particle of diameter 4 mm. Initially, the partial pressures of He, and Ar are p_{10} = 0 kPa, p_{20} = 100 kPa, respectively. At time t = 0, the external surface is maintained at $p_{1,eq}$ = 100 kPa, $p_{2,eq}$ = 0 kPa. The time-evolution of the partial pressures, and total pressures are shown. The continuous solid lines are the calculations using the DGM equation (**5**). Input data in Table S**2**.

Figure S18. Transient uptake inside particle made of mesoporous Vycor glass exposed to a gas phase $He_2(1)/N_2(2)$ mixture at 293 K. Initially, the particle is equilibrated with partial pressures are p_1 = 50 kPa; p_2 = 50 kPa. For times, $t \geq 0$, the partial pressures of the components in the bulk gas phase are maintained at p_1 = 100 kPa; p_2 = 0 kPa. The structural data are provided in Table S3.

Figure S19. Experimental data of Tuchlenski et al.[9] for the dynamic pressure increase in the downstream compartment (data scanned from Figure 7a and Figure 7b of Tuchlenski paper) for (a) He-CO_2 mixtures at 293 K, and (b) He-CO_2 mixtures at 343 K. The continuous solid lines are the calculations using the DGM equation (5). The dashed lines are the calculations using the M-S equation (25), taking $Đ_{He} = D_{He,Kn}$ and $Đ_{CO2} = 0.55 D_{CO2,Kn}$ in (a) $Đ_{He} = D_{He,Kn}$ and $Đ_{CO2} = 0.7 D_{CO2,Kn}$ in (b). Input data in Table S2.

Figure S20. Experimental data of Tuchlenski et al.[9] for the dynamic pressure increase in the downstream compartment (data scanned from Figure 7c and Figure 7d of Tuchlenski paper) for (a) He-C_3H_8 mixtures at 293 K, and (b) He-C_3H_8 mixtures at 343 K. The continuous solid lines are the calculations using the DGM equation (5). The dashed lines are the calculations using the M-S equation (25), taking $Đ_{He} = D_{He,Kn}$ and $Đ_{C3H8} = 0.78 D_{C3H8,Kn}$ in (a) $Đ_{He} = D_{He,Kn}$ and $Đ_{C3H8} = 0.87 D_{C3H8,Kn}$ in (b). Input data in Table S2.

Figure S21. Experimental data of Tuchlenski et al.[9] for the dynamic pressure increase in the downstream compartment (data scanned from Figure 10 of Tuchlenski paper) for CO_2-C_3H_8 mixtures at 293 K. The continuous solid lines are the calculations using the DGM equation (5). The dashed lines are

the calculations using the M-S equation (25), taking $Đ_{CO2} = 0.55D_{CO2,Kn}$ and $Đ_{C3H8} = 0.78D_{C3H8,Kn}$. Input data in Table S2.

Figure S22. Experimental data of Tuchlenski et al.[9] for the dynamic pressure increase in the downstream compartment, initially filled with CO_2, for CO_2-C_3H_8 mixtures at 293 K. Comparison with M-S model calculations taking $Đ_{C3H8} = 0.78D_{C3H8,Kn}$, along with different values of $Đ_{CO2}$ as specified in the Figure 22.

Figure S23. (a) Comparing the transmembrane fluxes calculated by the DGM (continuous solid lines) and Maxwell-Stefan (dashed lines) models for the Tuchlenski experiments for CO_2-C_3H_8 mixtures at 293 K in which the downstream compartment is initially filled with CO_2, and the upstream compartment is maintained at constant composition with a 1:1 CO_2-C_3H_8 mixture at 10^5 Pa. (b) Calculations of the component permeances Π_i using the DGM and M-S model calculations.

Figure S24. Experimental data of Yang et al.[27] for the dynamic pressure increase in the downstream compartment (data scanned from Figure 5 of Yang paper) for He-CO_2 mixtures at 293 K. The continuous solid lines are the calculations using the DGM equation (5). The dashed lines are the calculations using the M-S equation (25), taking $Đ_{He} = D_{He,Kn}$ and $Đ_{CO2} = 0.55D_{CO2,Kn}$. Input data in Table S3.

Figure S25. Experimental data of Yang et al.[27] for the dynamic pressure increase in the downstream compartment (data scanned from Figure 6 of Yang paper) for CO_2-C_3H_8 mixtures at 293 K. The continuous solid lines are the calculations using the DGM equation (5). The dashed lines are the calculations using the M-S equation (25), taking $Đ_{CO2} = 0.55 D_{CO2,Kn}$ and $Đ_{C3H8} = 0.88 D_{C3H8,Kn}$. Input data in Table S3.

Figure S26. (a) Comparing the transmembrane fluxes calculated by the DGM (continuous solid lines) and Maxwell-Stefan (dashed lines) models for the Yang experiments for CO_2-C_3H_8 mixtures at 293 K in which the downstream compartment is initially filled with CO_2, and the upstream compartment is flushed with pure C_3H_8 at 10^5 Pa. (b) Calculations of the component permeances Π_i using the DGM and M-S model calculations.

Figure S27. Ratio $Đ_i/D_{i,Kn}$, obtained from the simulations of Tuchlenski and Yang experiments plotted as a function of the Henry coefficient for adsorption. The Henry coefficient is determined from the Langmuir constants for the unary isotherms as reported in Table 2 of Tuchlenski et al.[9] and Table 1 of Yang et al.[27] The Henry coefficients are calculated as the product of the saturation capacity, $c_{i,sat}$ (units: mol m^{-3}), and the Langmuir constant, b_i (units: Pa^{-1}), divided by the skeletal density, ρ (= 2057 kg m^{-3}).

Please note that the isotherm data reported by Tuchlenski and Yang use c_i defined in terms of mol of species i per m^3 of solid material; for this reason we use the skeletal density in the calculation of the Henry constant.

Figure S28. Experimental data of Veldsink et al.[28] for the dynamic pressure increase in the downstream compartment (data scanned from Figure 12 and Figure 13 of Veldsink paper) for (a) He-CO_2 mixtures at

293 K, and (b) He-CO_2 mixtures at 434 K. The continuous solid lines are the calculations using the DGM equation (5). The dashed lines are the calculations using the M-S equation (25), taking $Đ_{He} = D_{He,Kn}$ and $Đ_{CO2} = 0.85 D_{CO2,Kn}$ in (a) and $Đ_{He} = D_{He,Kn}$ and $Đ_{CO2} = 0.9 D_{CO2,Kn}$ in (b). Input data in Table S4.

Figure S29. Experimental data of Veldsink et al.[28] for the dynamic pressure increase in the downstream compartment (data scanned from Figure 14 and Figure 15 of Veldsink paper) for (a) He-C_3H_8 mixtures at 293 K, and (b) He-C_3H_8 mixtures at 416 K. The continuous solid lines are the calculations using the DGM equation (5). The dashed lines are the calculations using the M-S equation (25), taking $Đ_{He} = D_{He,Kn}$ and $Đ_{C3H8} = 0.95 D_{C3H8,Kn}$ in (a) and $Đ_{He} = D_{He,Kn}$ and $Đ_{C3H8} = 0.98 D_{C3H8,Kn}$ in (b). Input data in Table S4.

Figure S30. Experimental data of Tuchlenski et al.[9] for the dynamic pressure increase in the downstream compartment for CO_2-C_3H_8 mixtures at 293 K. Comparison of mesopore diffusion model with surface diffusion model.

Figure S31. Experimental data of Yang et al.[27] for the dynamic pressure increase in the downstream compartment for CO_2-C_3H_8 mixtures (data scanned from Figure 6 of Yang paper) at 293 K. Comparison of mesopore diffusion model with surface diffusion model.

Figure S32. Experimental data of Yang et al.[27] for the dynamic pressure increase in the downstream compartment for CO_2-C_3H_8 mixtures (data scanned from Figure 7 of Yang paper) at 293 K. Comparison with surface diffusion model.

Figure S1

The Dusty Gas Model

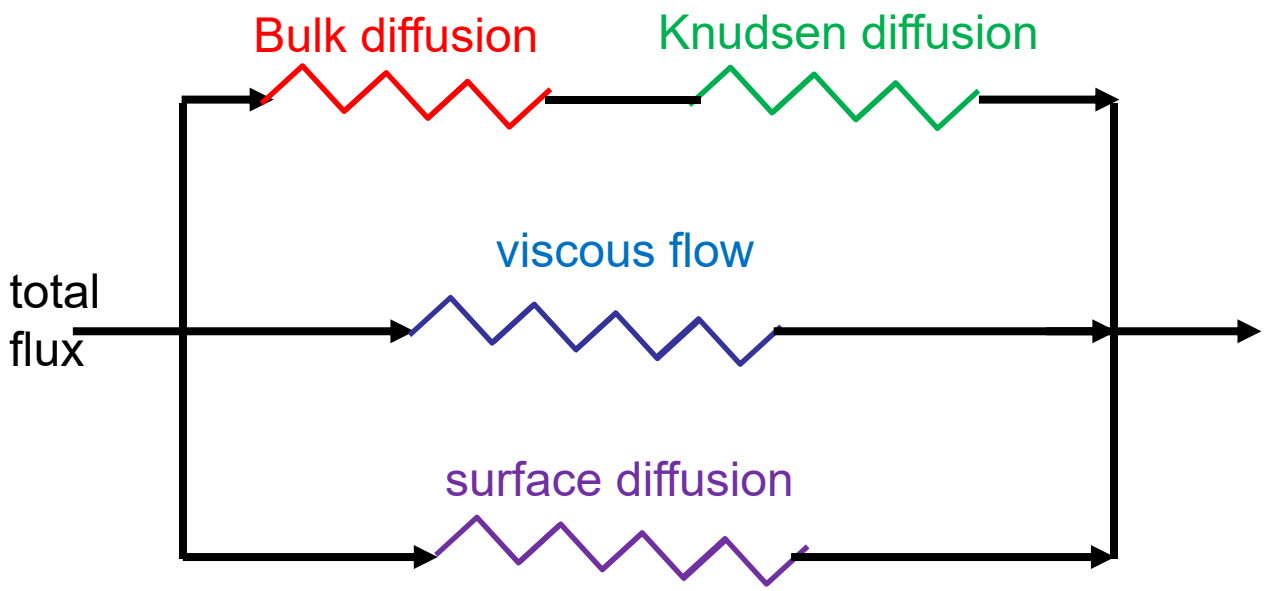

Figure S2

Knudsen and bulk diffusivities

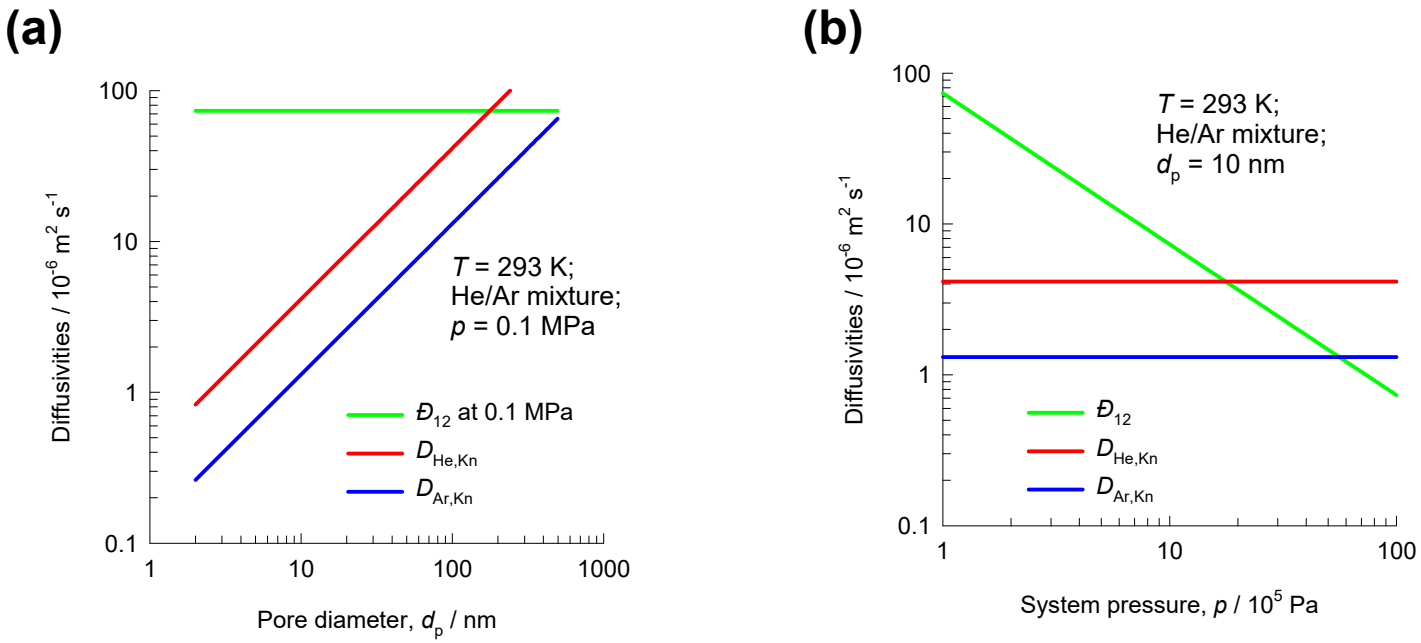

Figure S3

Linearized DGM vs Remick Expt

(a)

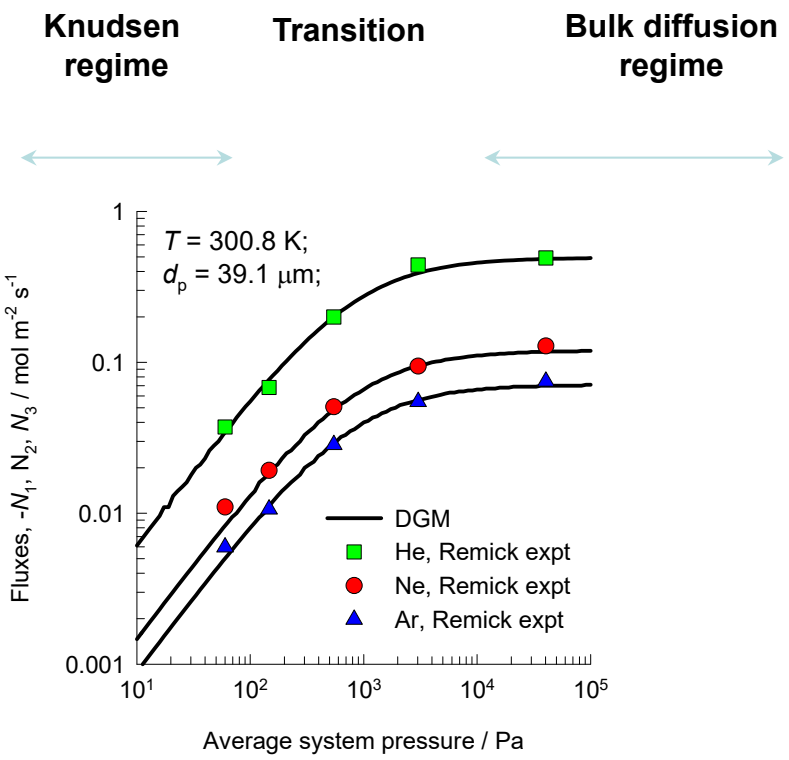

(b)

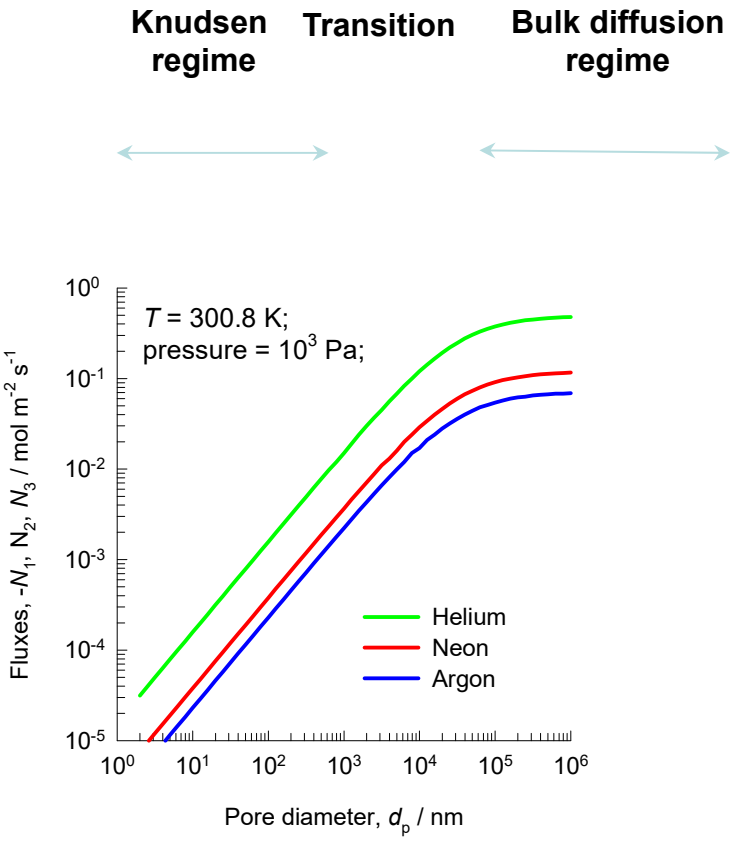

Figure S4

Combining Knudsen, Viscous flow and Surface diffusion

(a)

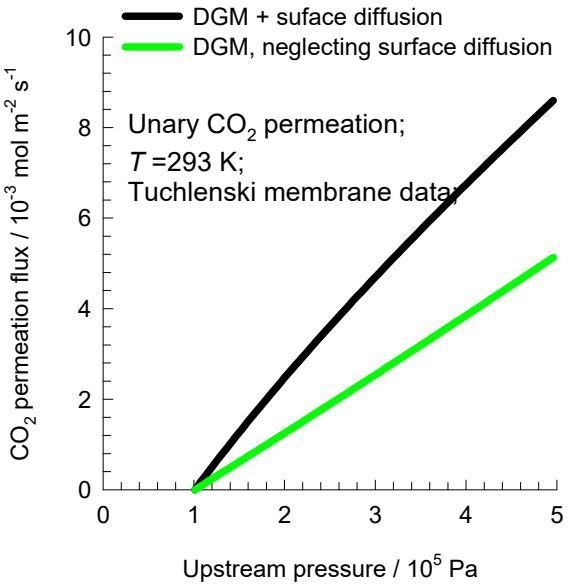

(b)

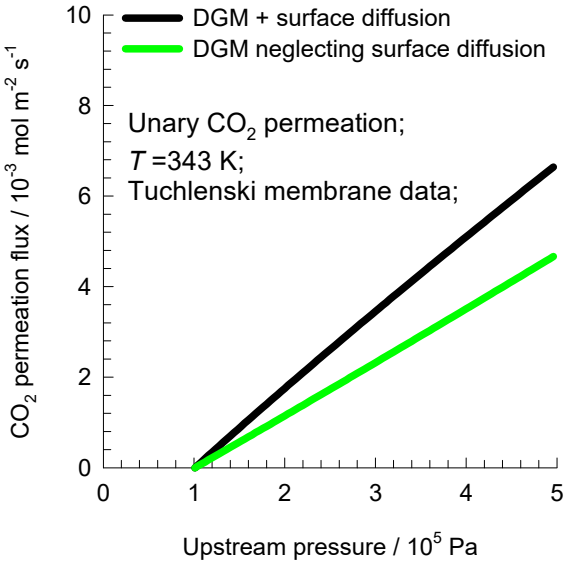

Figure S5

Molecule-Molecule interactions

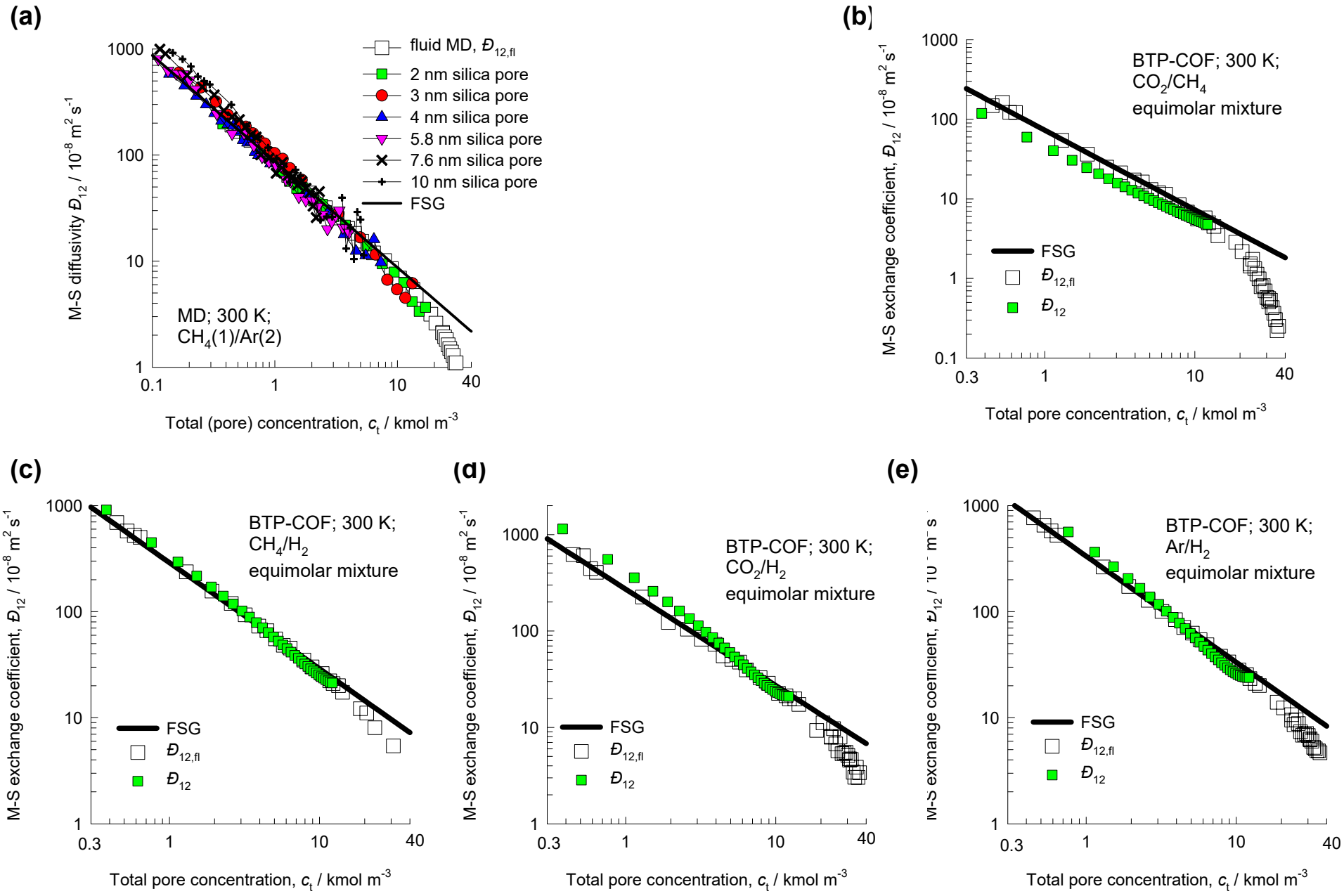

Figure S6

Molecule-Wall interactions

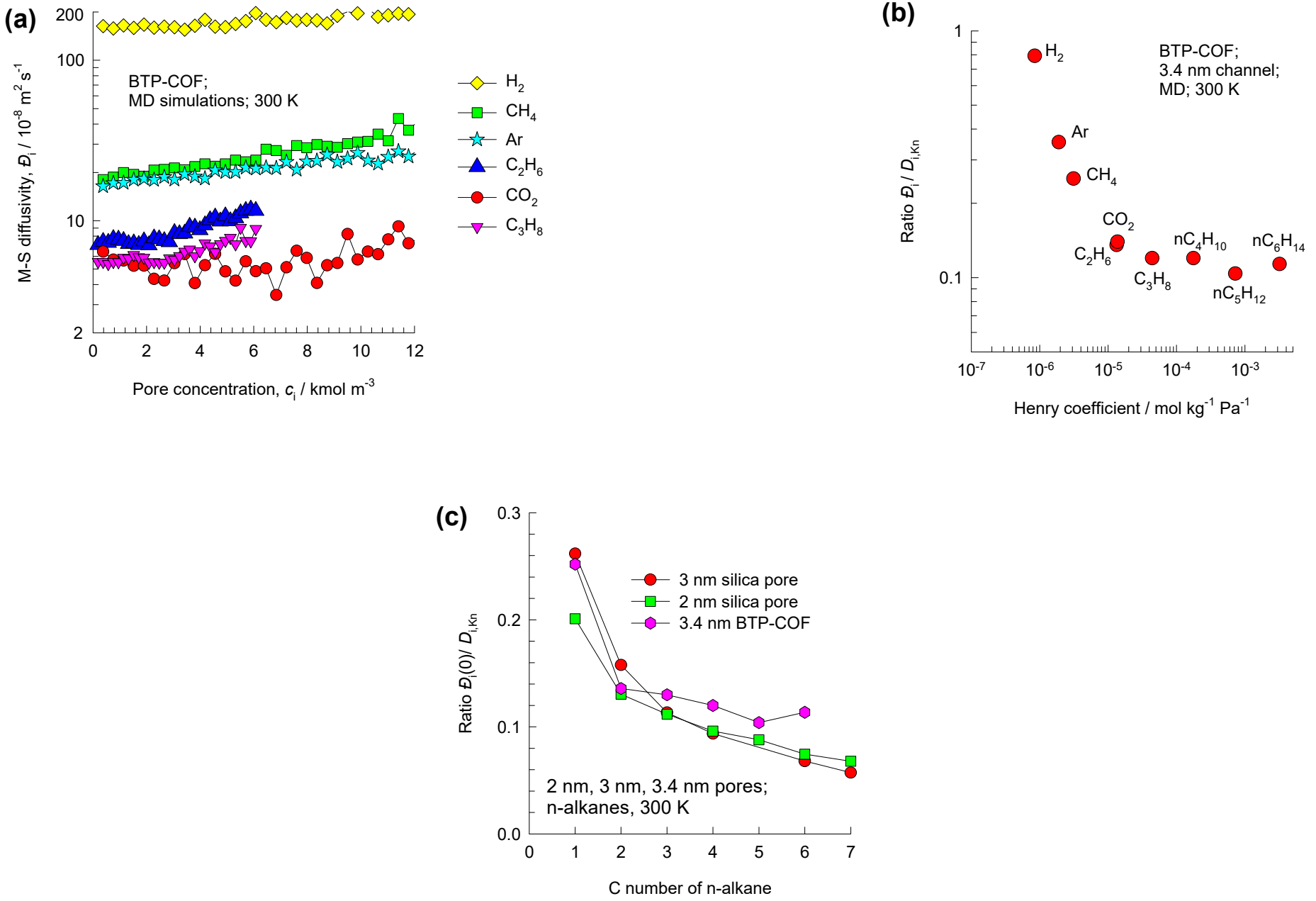

Figure S7

Molecule-Wall interactions

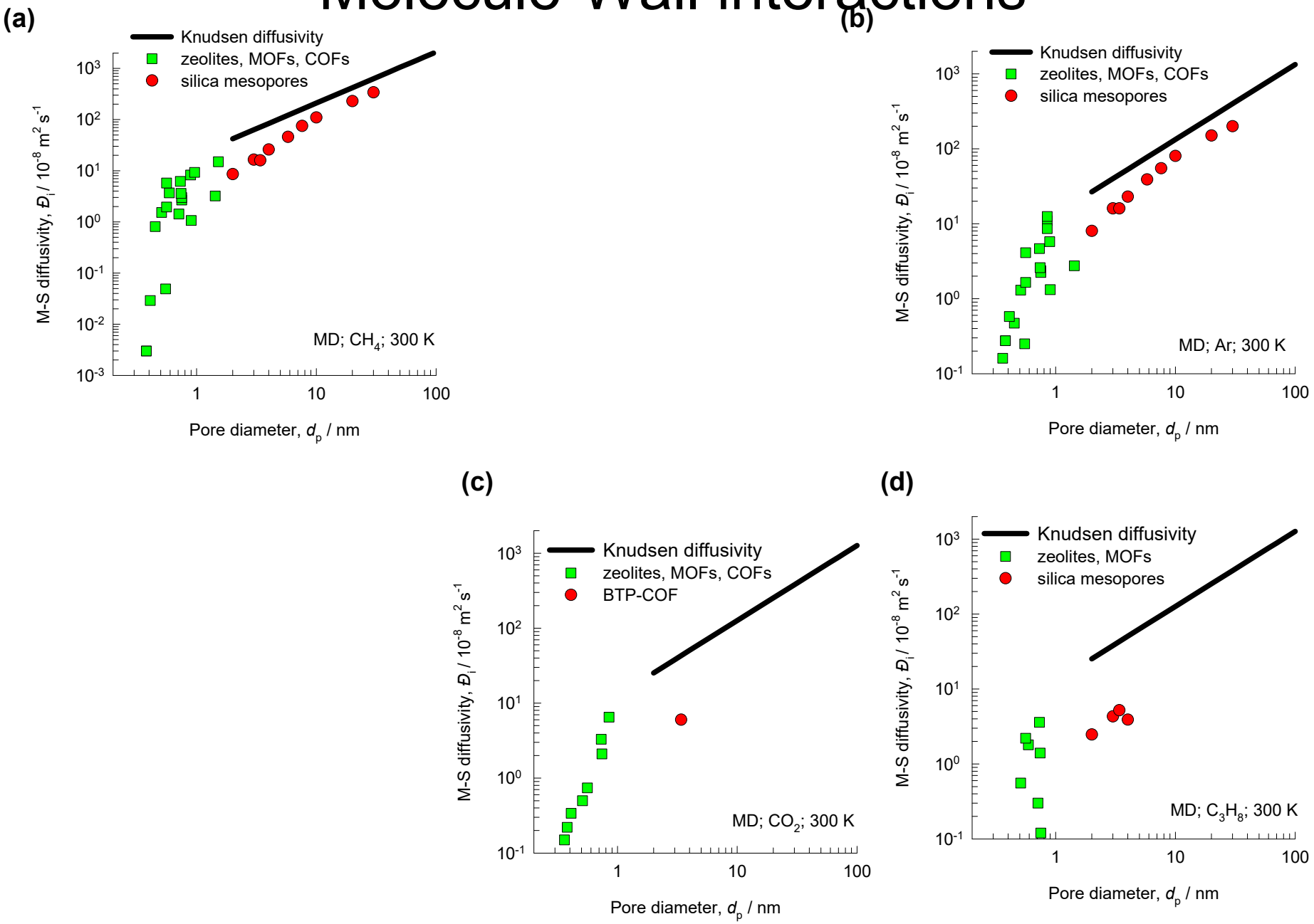

Figure S8

$H_2/N_2/CO_2$ gas mixture diffusion

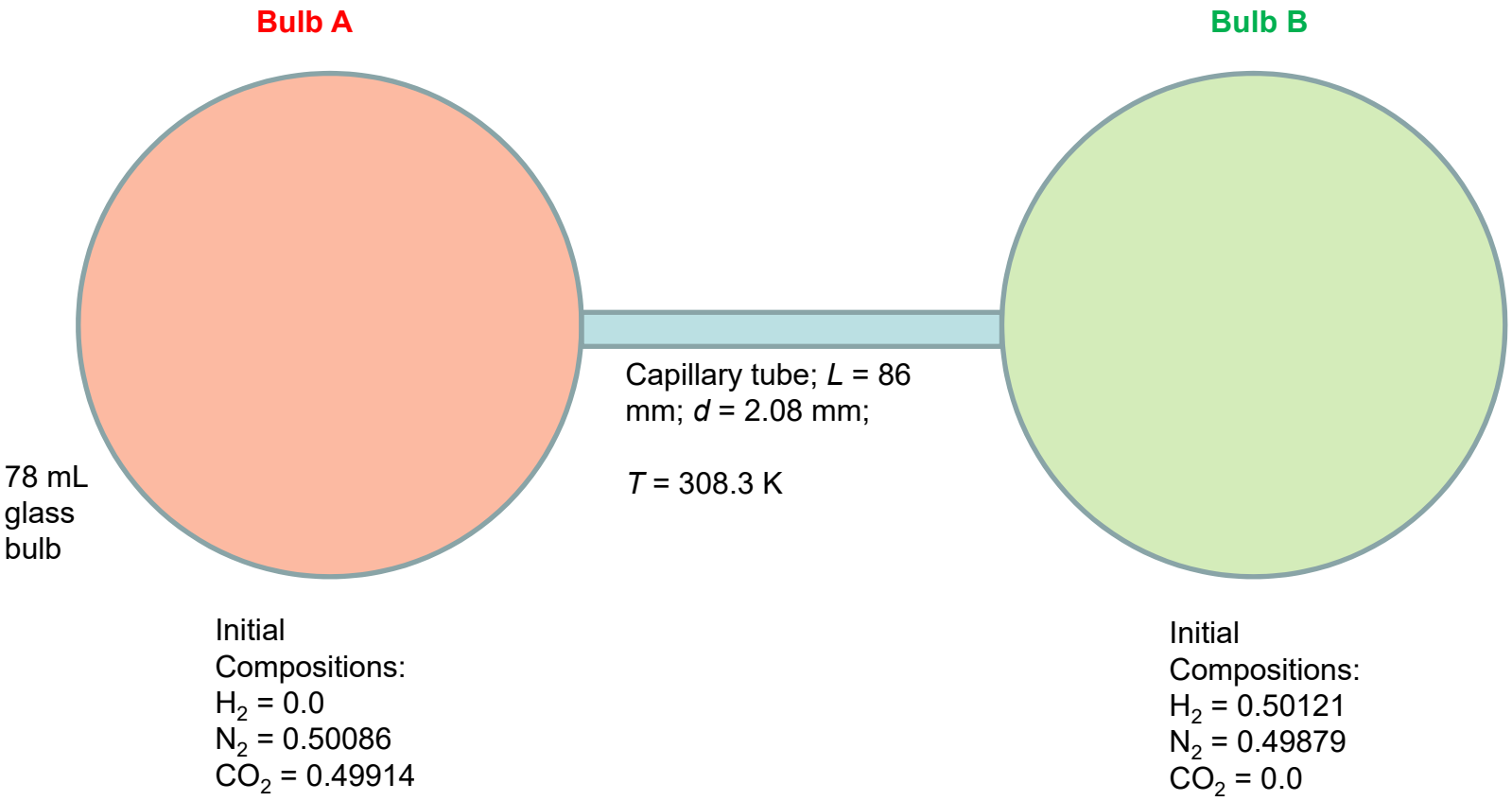

Figure S9

$H_2/N_2/CO_2$ gas mixture diffusion

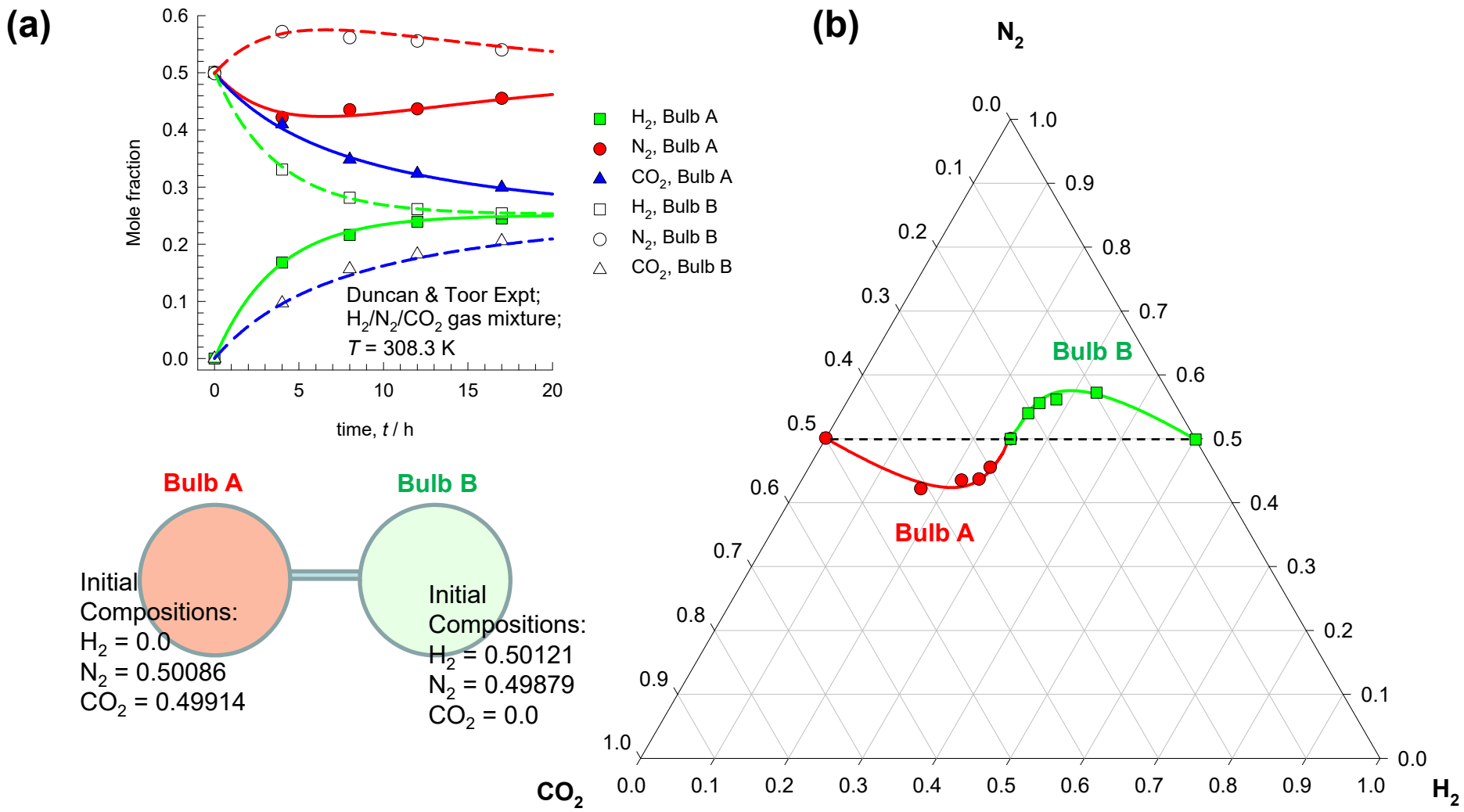

Figure S10

$H_2/N_2/CO_2$ gas mixture diffusion

(a)

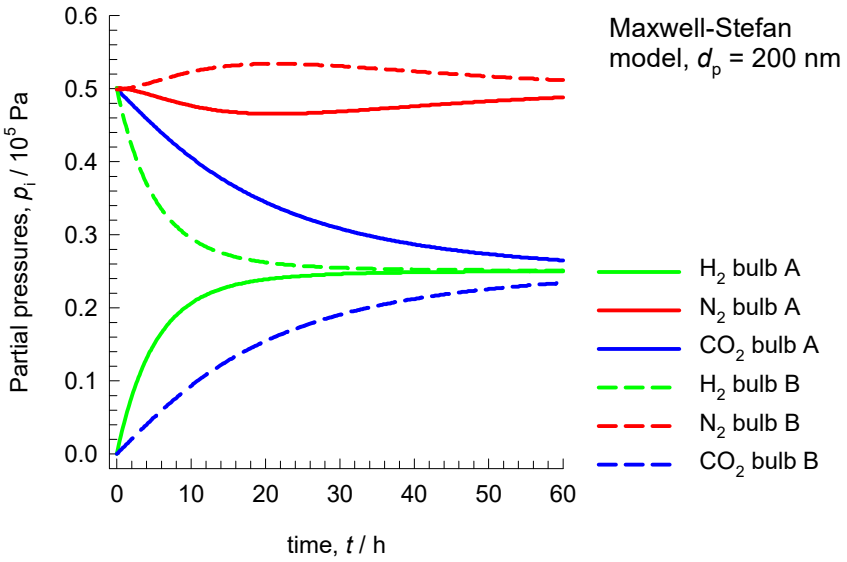

(b)

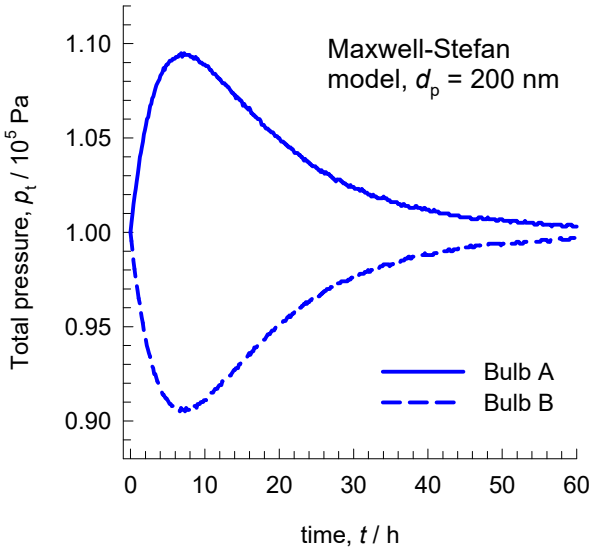

Figure S11

$H_2/N_2/CO_2$ gas mixture diffusion

(a)

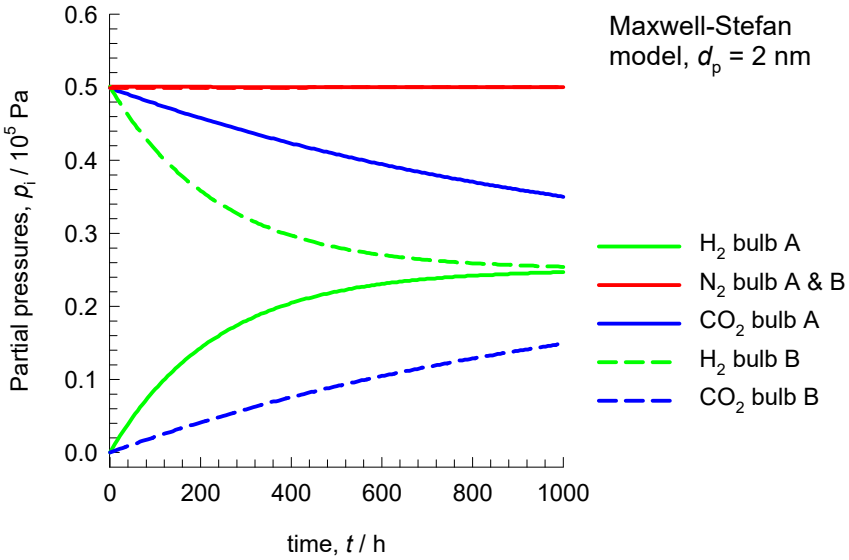

(b)

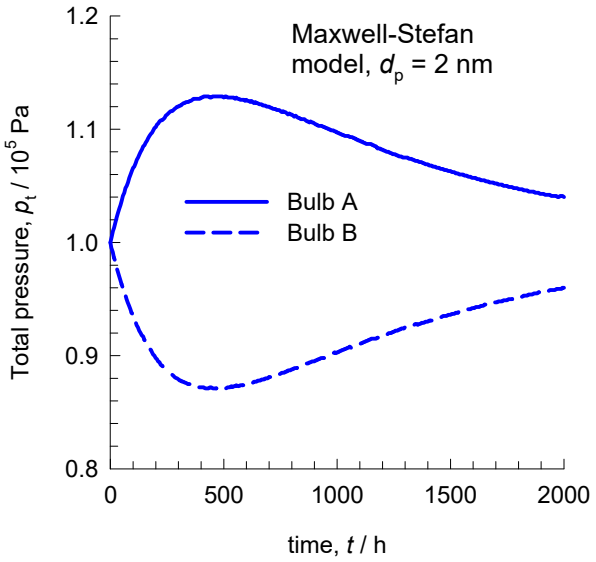

Figure S12

$H_2/N_2/CO_2$ gas mixture diffusion

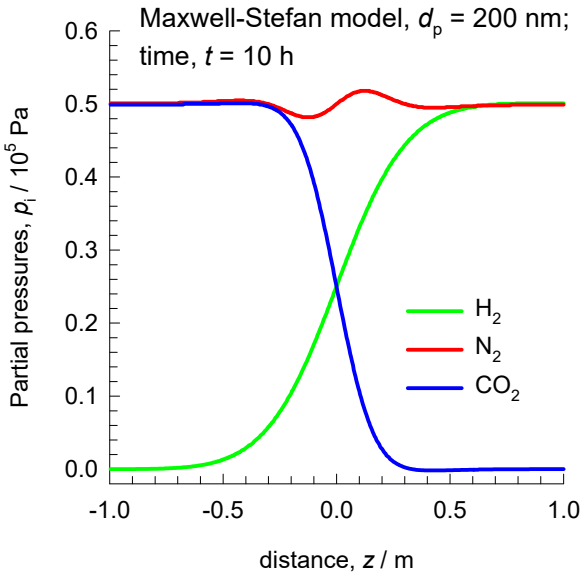

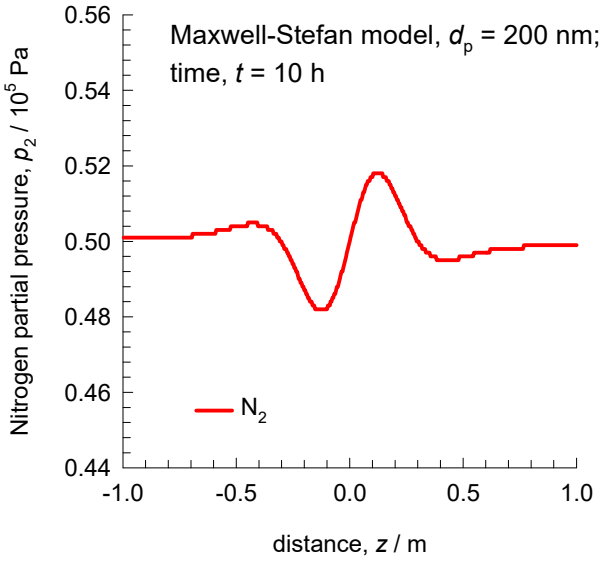

Figure S13

Velsink, Tuchlenski, and Yang expt set-ups

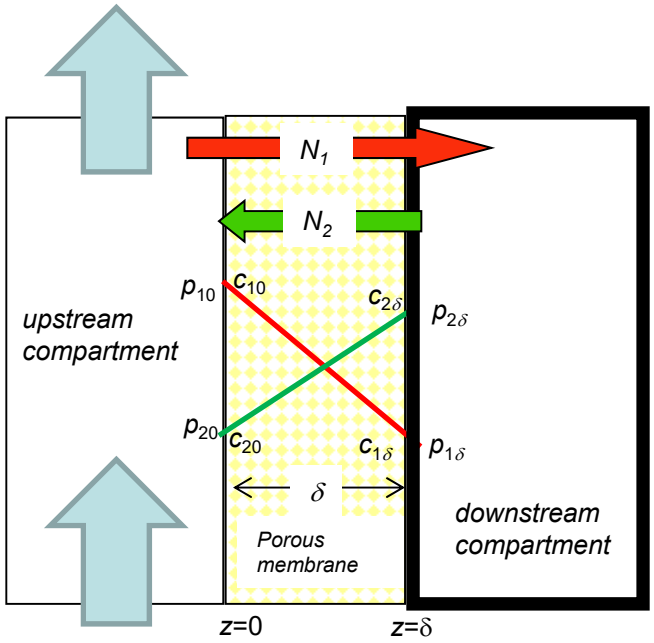

Figure S14

Tuchlenski transient experiments

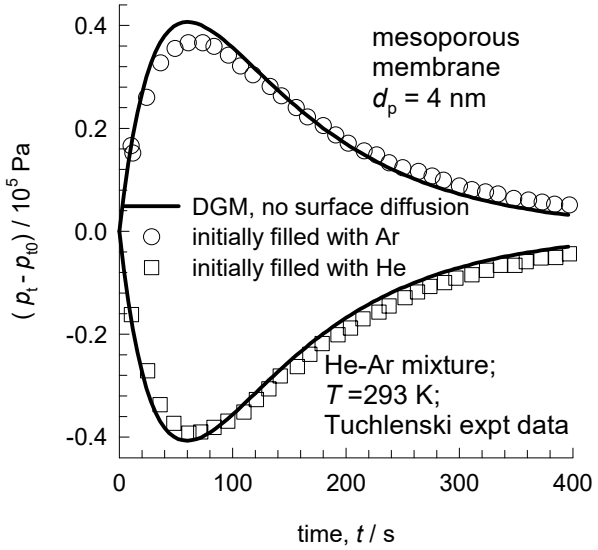

Figure S15

Yang transient experiments

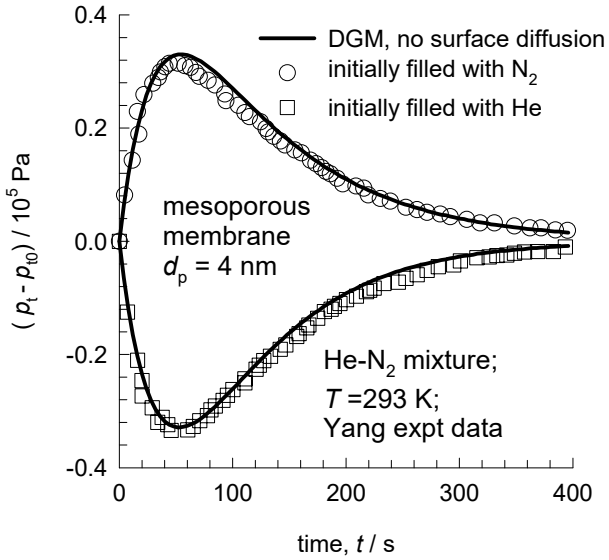

Figure S16

Veldsink transient experiments

(a)

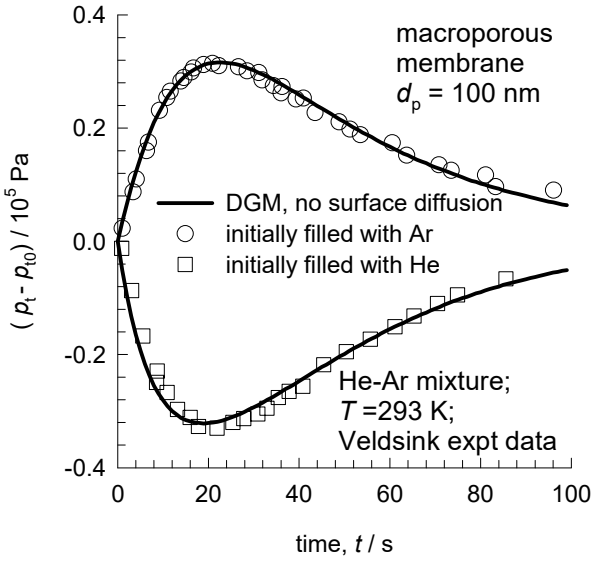

(b)

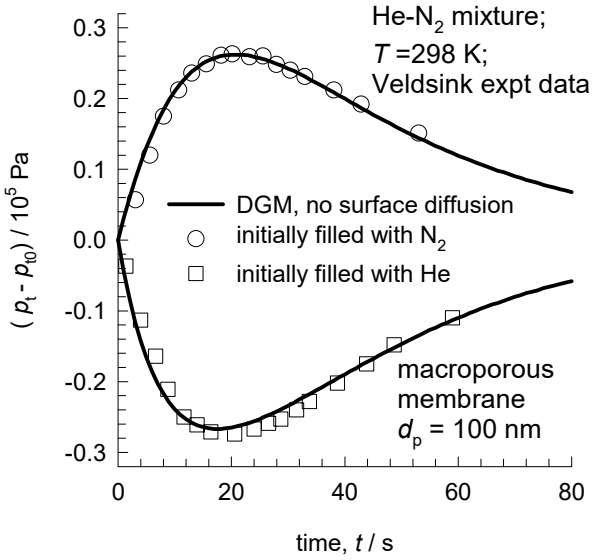

Figure S17

Transient uptake inside particles

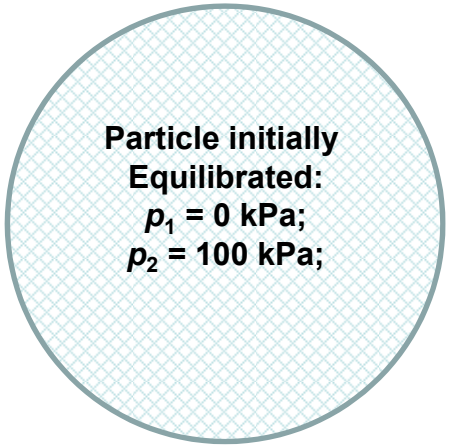

Bulk maintained at:
p_1 = 100 kPa;
p_2 = 0 kPa;

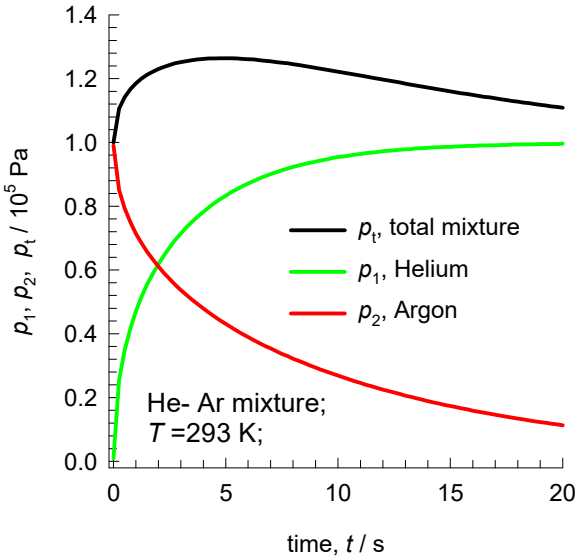

Figure S18

Total pressure overshoot: mesoporous particle

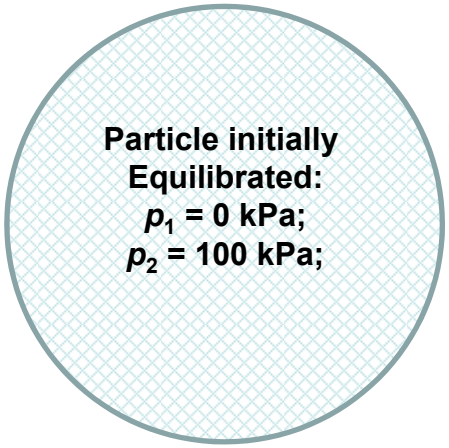

Bulk maintained at:
p_1 = 100 kPa;
p_2 = 0 kPa;

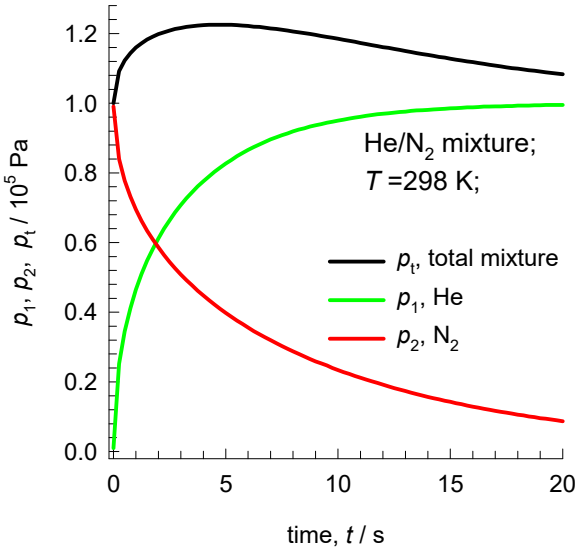

Figure S19

Tuchlenski transient experiments

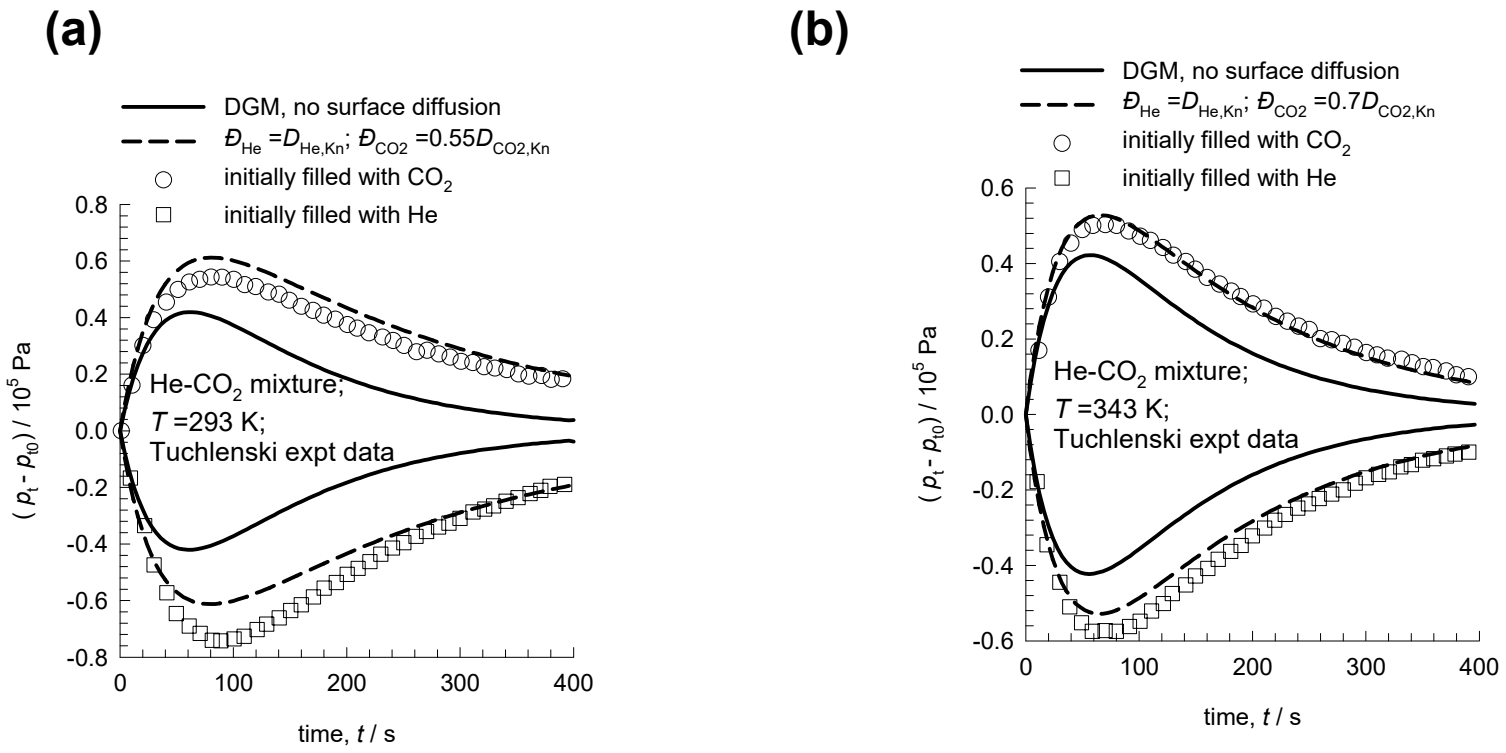

Figure S20

Tuchlenski transient experiments

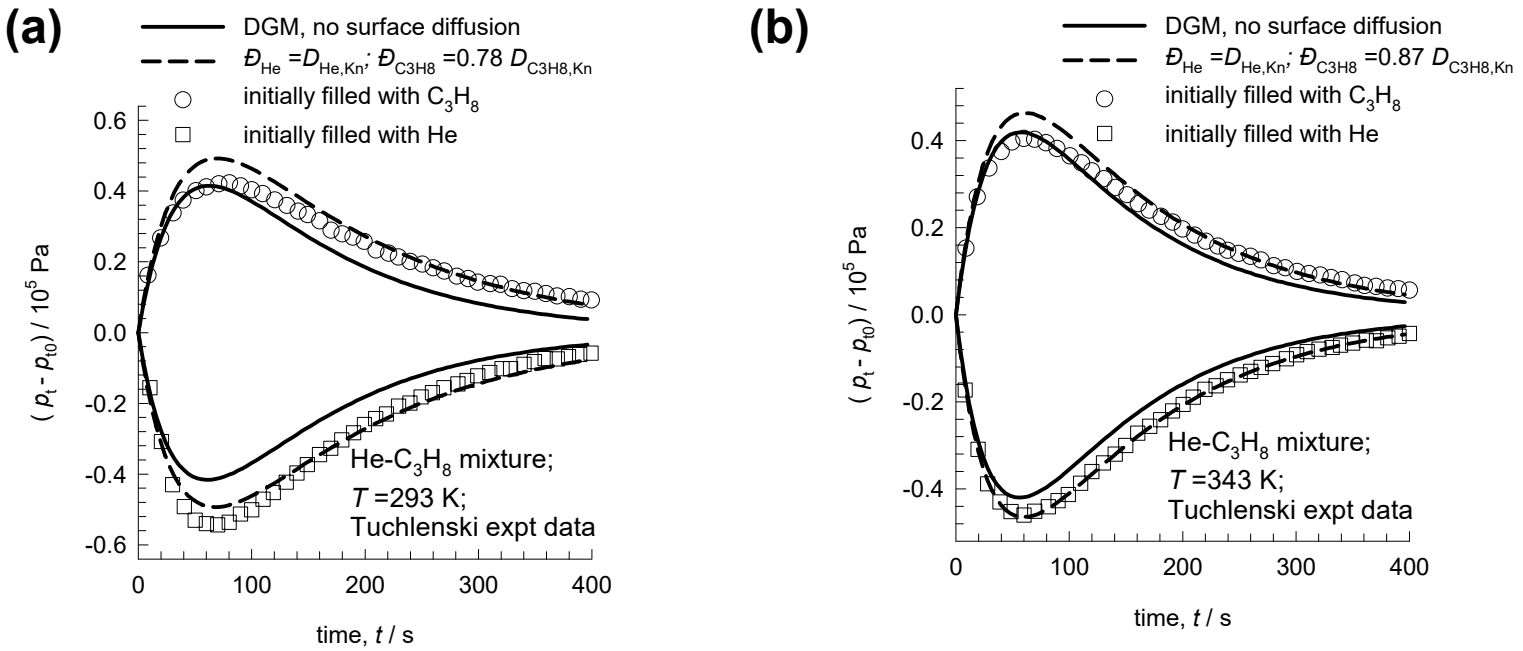

Figure S21

Tuchlenski transient experiments

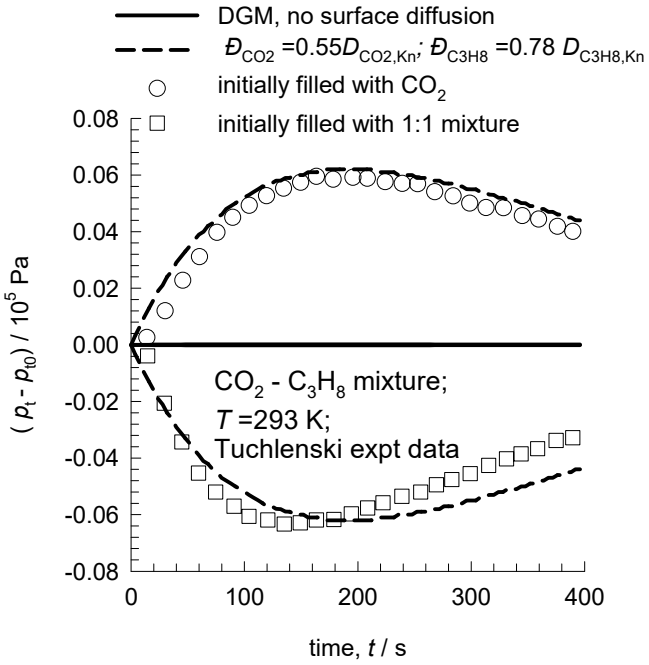

Figure S22

Tuchlenski transient experiments

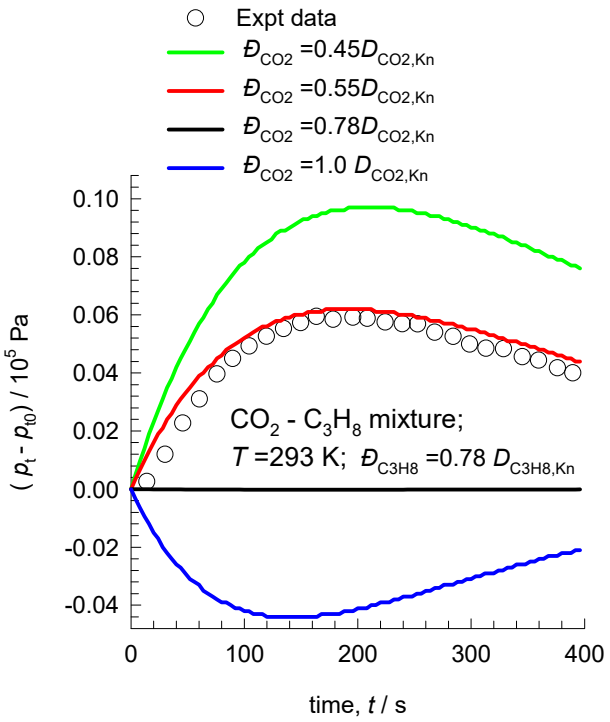

Figure S23

Tuchlenski transient experiments

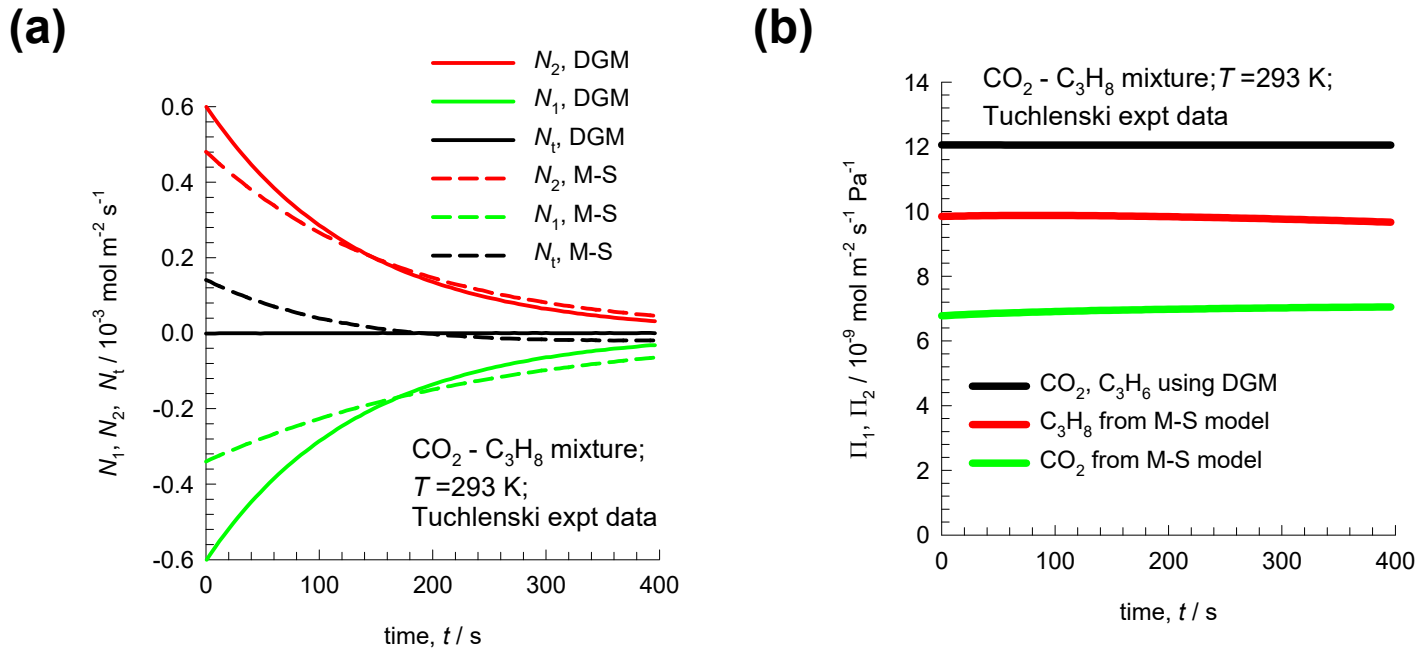

Figure S24

Transient Yang experiments

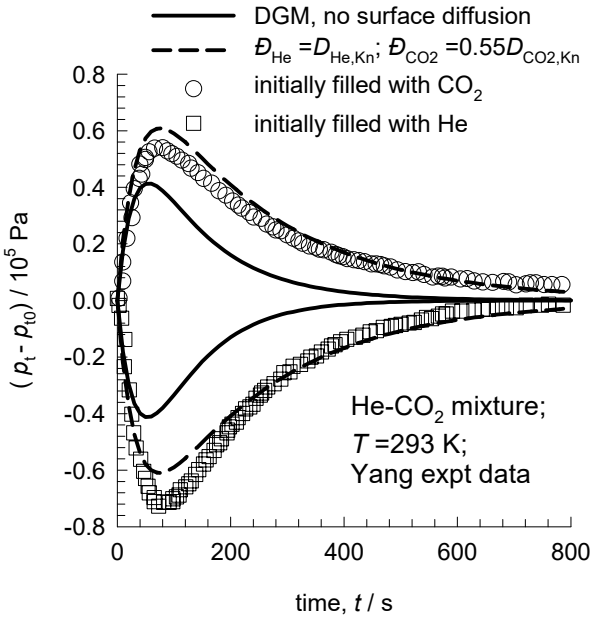

Figure S25

Transient Yang experiments

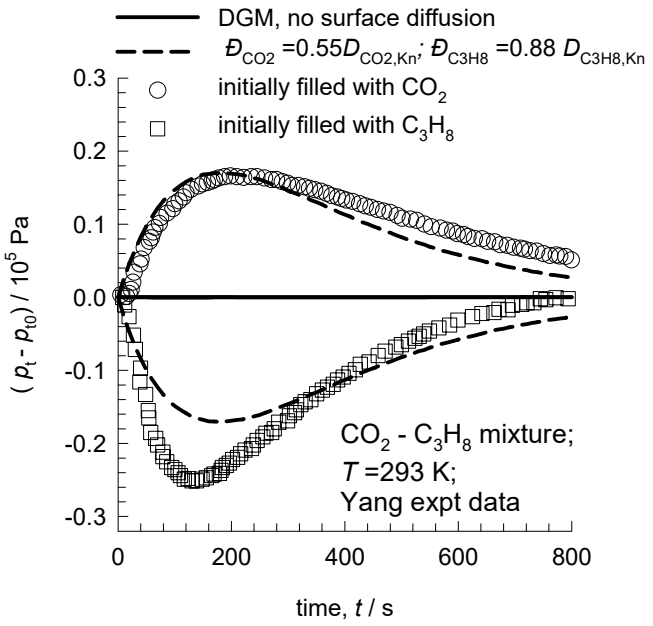

Figure S26

Transient Yang experiments

(a)

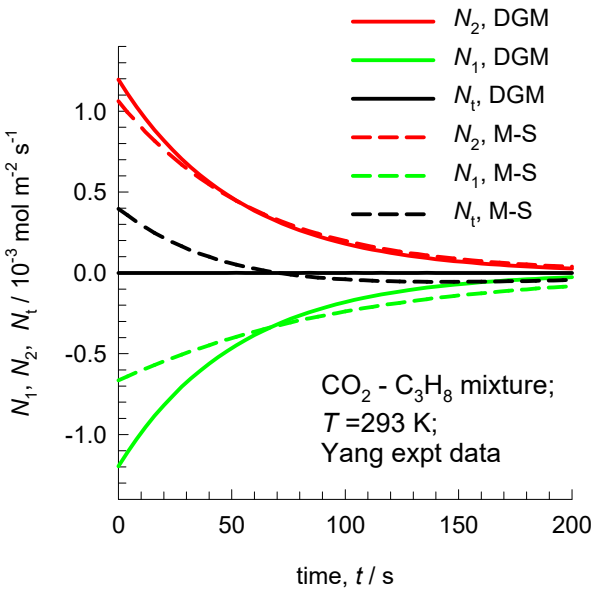

(b)

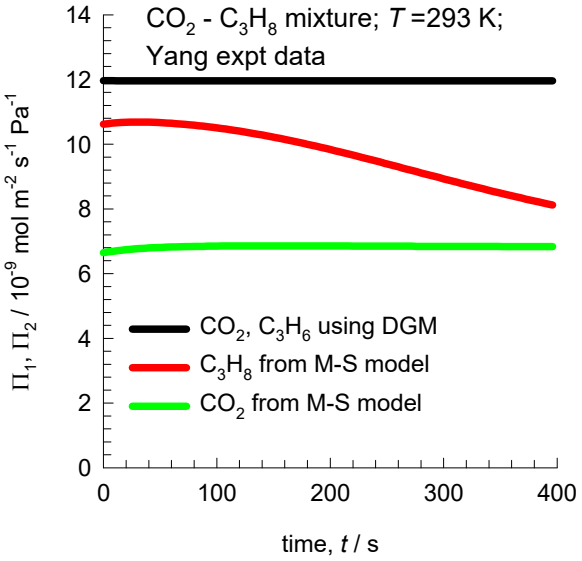

Influence of adsorption on molecule-wall interactions

Figure S27

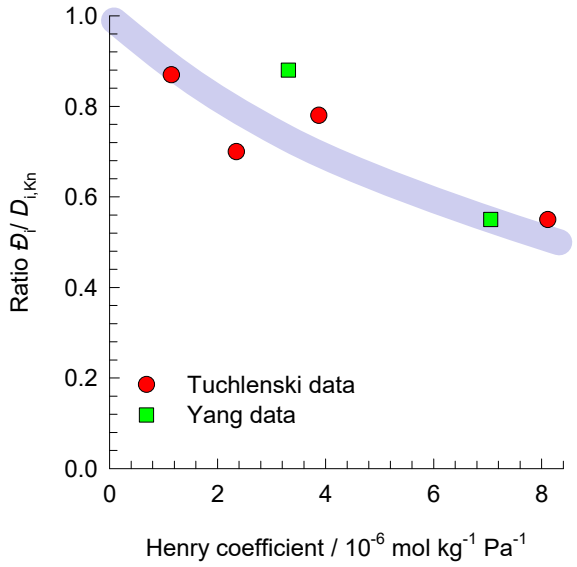

Figure S28

Veldsink transient experiments

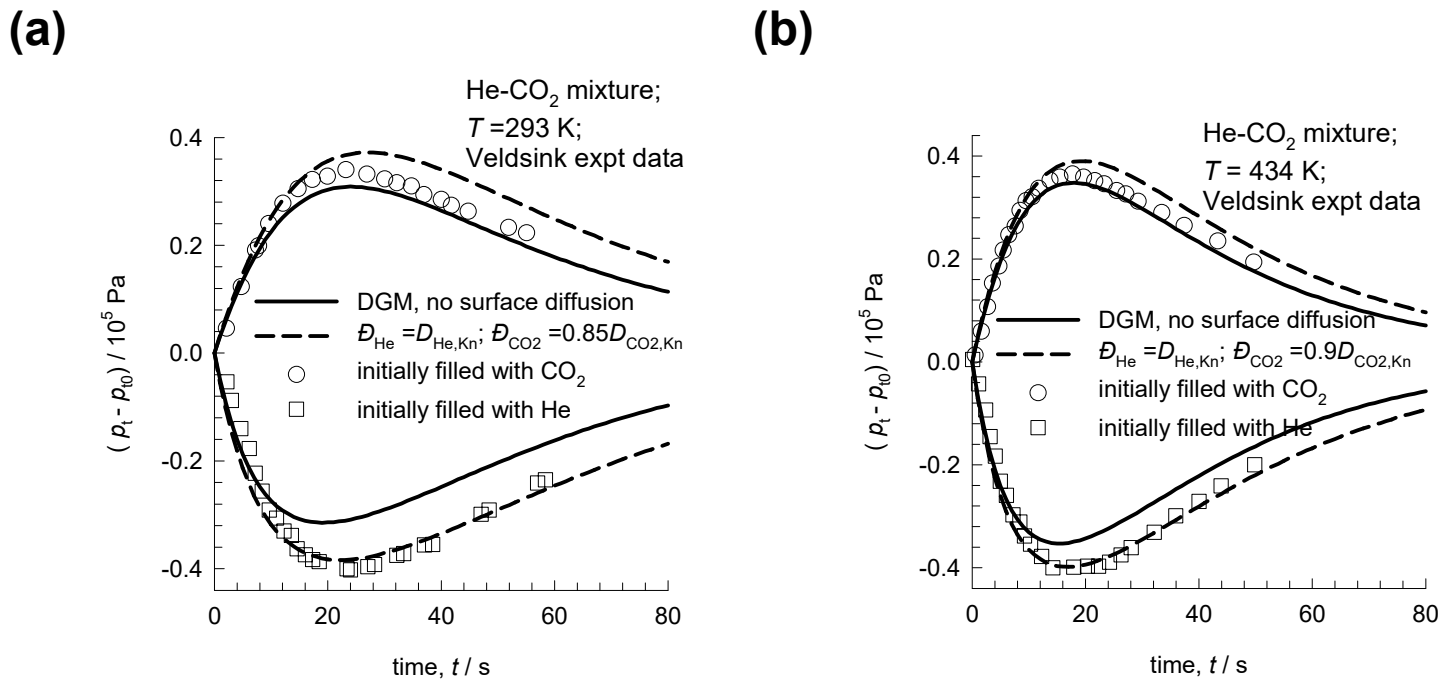

Figure S29

Veldsink transient experiments

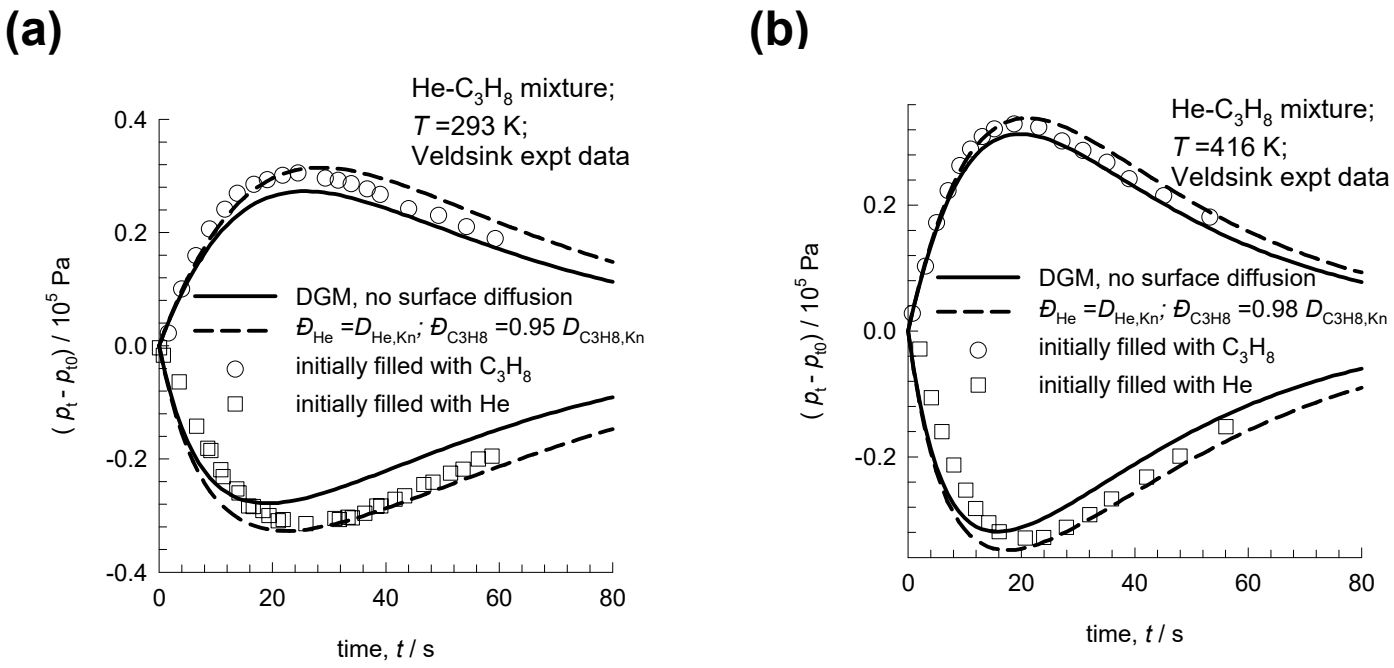

Figure S30

Surface diffusion model for Tuchlenski expts

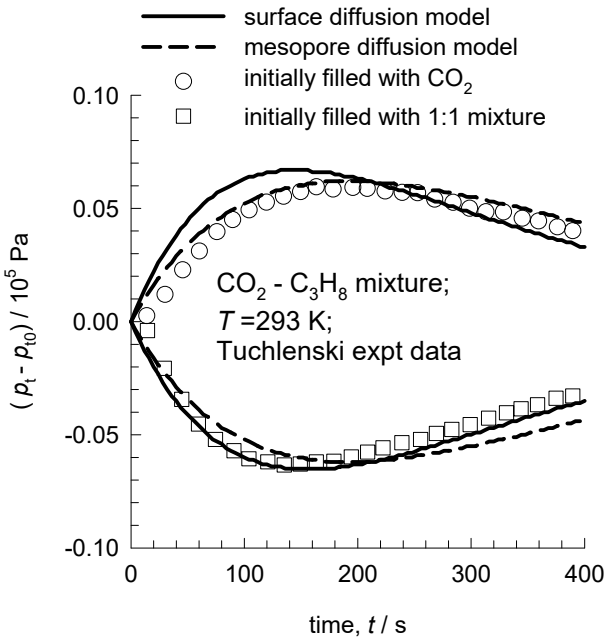

Figure S31

Surface diffusion model for Yang expts

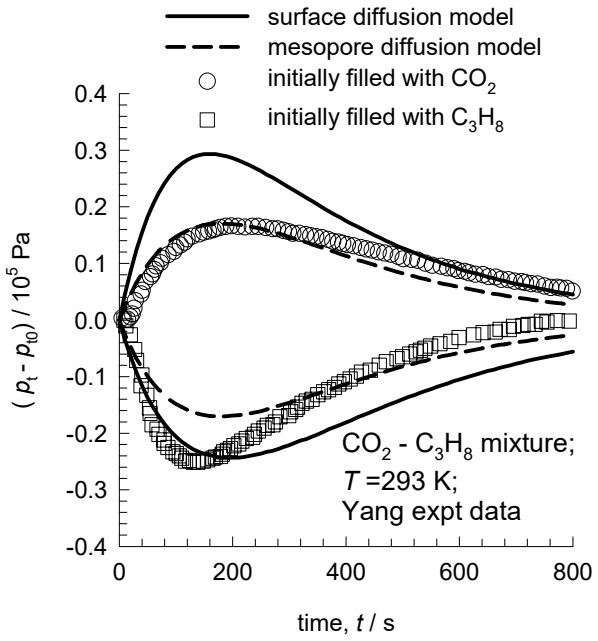

Figure S32

Surface diffusion model for Yang expts